AMERICAN SCIENCE AND ENGINEERING

11 CARLETON STREET, CAMBRIDGE,
MASSACHUSETTS 02142 (617) 868-1600

JUNE 1970

ASE-2455

FINAL REPORT

GRAZING-INCIDENCE TELESCOPES FOR CELESTIAL X-RAY ASTRONOMY USING AEROBEE ROCKETS

CONTRACT NASW-1758

PREPARED FOR

NATIONAL AERONAUTICS
AND SPACE ADMINISTRATION
WASHINGTON, D.C. 20546

ASE-2455

Final Report:

GRAZING-INCIDENCE TELESCOPES FOR CELESTIAL X-RAY ASTRONOMY USING AEROBEE ROCKETS

Contract NASW-1758

Prepared for:

National Aeronautics & Space Administration
Washington, D.C. 20546

By:

American Science & Engineering, Inc.
11 Carleton Street
Cambridge, Massachusetts 02142

June 1970

Approved: _____
H. Gursky
Principal Investigator

Approved: _____
R. Giacconi
Executive Vice President

CONTENTS

1.0 INTRODUCTION

The work described in this report is entirely related to celestial x-ray astronomy using grazing-incidence telescopes in Aerobee Sounding rockets. We describe the Aerobee-150 payload which was built by AS&E and flown on 6 February 1970 aboard NASA Flight 4.262CG at White Sands, N. M. This payload contained a 9.5-inch x-ray telescope system for observing celestial objects. Also reported on is some basic research AS&E has performed with optical surfaces, measuring their x-ray reflecting properties. This work will be useful in constructing future, improved telescopes.

Finally, a design study performed by AS&E is reported, in which a grazing-incidence telescope was incorporated into an Aerobee-350 payload. The only problem seen with this approach is the lack of precise roll-axis stabilization when using NASA's presently configured STRAP III pointing system in the offset mode. AS&E believes this can be solved by adding a roll-axis stabilizer to the basic STRAP III System.

2.0 PAYLOAD DESCRIPTION

2.1 OVERALL SYSTEM

The three basic sections comprising the payload are the scientific instrumentation section, the attitude control section and the recovery section. Both the attitude control and recovery systems are government-furnished equipment and engineering details about these will not be presented in this report. Figure 2-1 shows the general configuration of the scientific portion of the payload. This contains a grazing-incidence telescope, an x-ray recording system, structures, payload electrical system, aspect optics and recording system, fine pointing sensor for attitude control, and telemetry.

General characteristics of the overall payload are as follows:

Overall length:	145 inches
Weight:	335 pounds
Diameter:	15 inches

Typical performance which may be expected is peak altitude of 530,000 feet at about 215 seconds using the Aerobee-150 vehicle.

2.2 PAYLOAD STRUCTURE

2.2.1 Nose Cone

The nose cone is .06 thick spun aluminum and has an included cone angle of 20 degrees. At approximately 70 km altitude, which corresponds to a time of 72 seconds, the nose cone is released exposing the x-ray telescope. The nose cone release system is shown in Figure 2-2. This system has been used by AS&E on previous flights and has proven to be reliable.

The release mechanism for the nose cone primarily consists of two rings held together by means of finger-like clamps which are held in the retentive position by a 1/8-inch dia. stainless steel flexible aircraft cable. Two guillotine cutters (for purposes of redundancy)

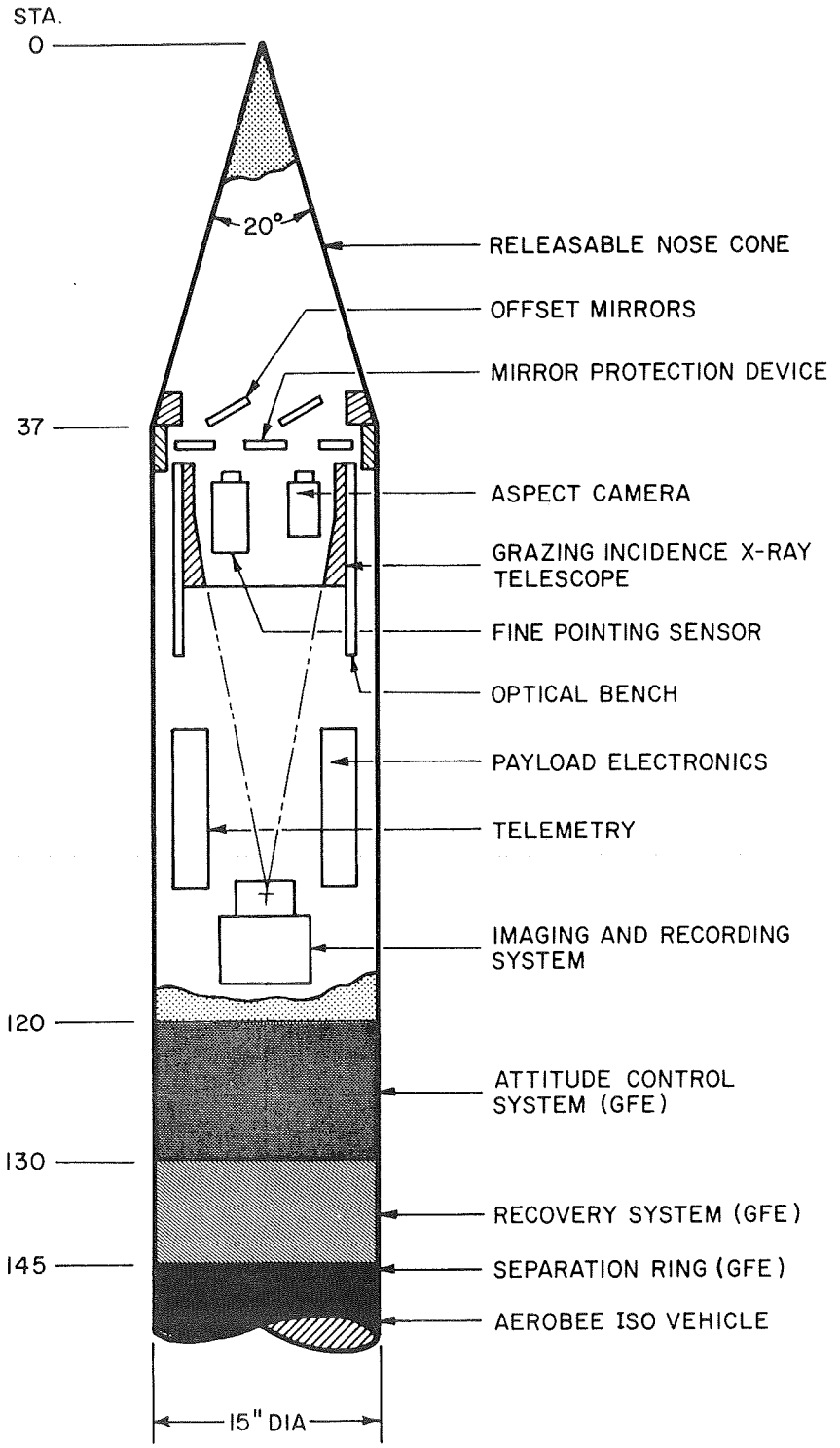

Figure 2-1 Layout of the rocket x-ray telescope experiment.

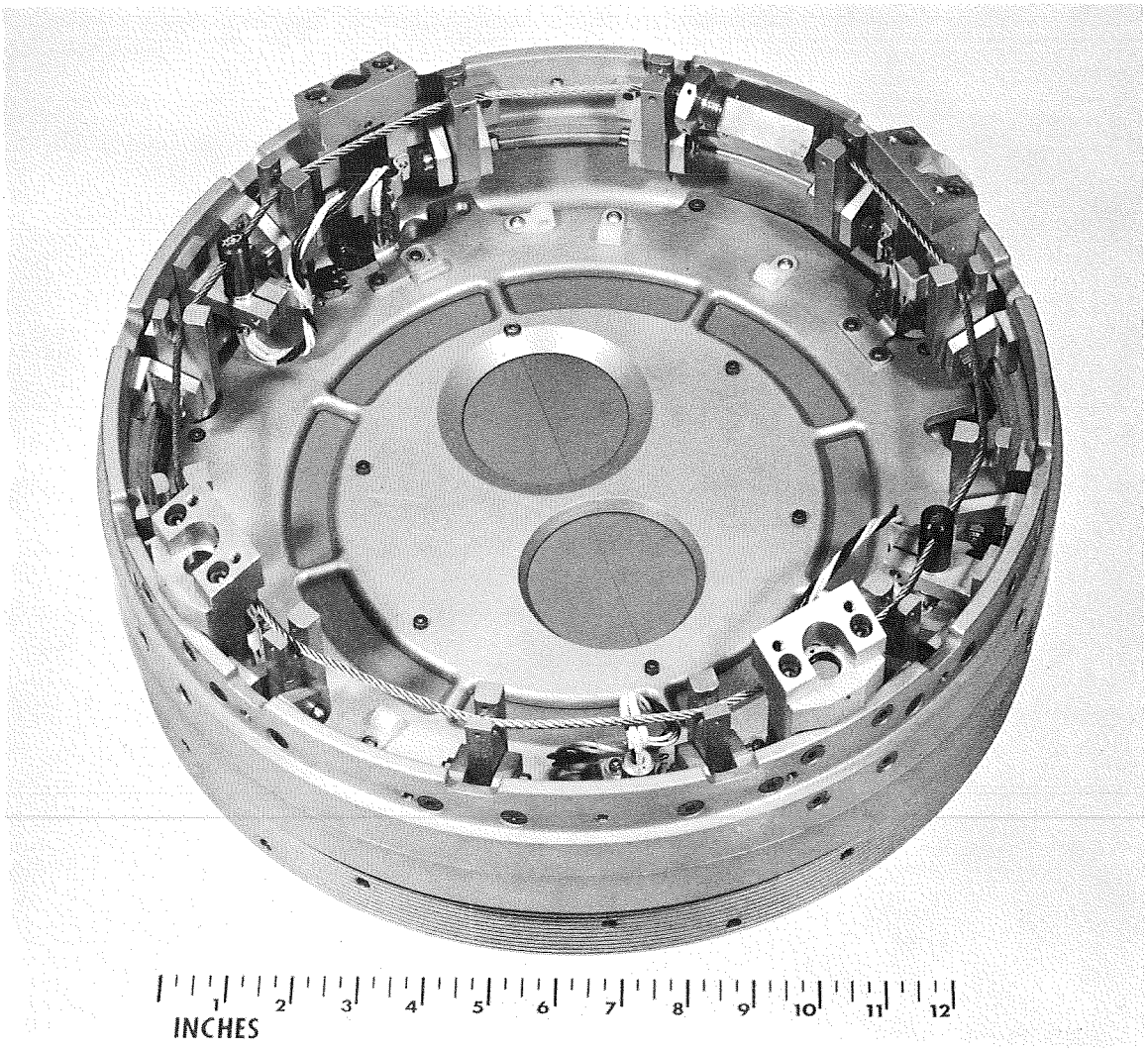

DZ-006

Figure 2-2 Eject assembly showing rings and protection devices.

are used to cut the cable and release the finger-clamps. Four compression springs then separate the two rings and impart a forward velocity of about 6 fps to the nose cone.

2.2.2 Optical Bench

An optical bench is used to maintain alignment between the x-ray telescope and the camera which record the image. The bench consists of four steel struts which attach to brackets on the telescope at the forward end. At the aft end, the image intensifier and camera system are attached by means of an adjustable bracket. This adjustment is required in order to position the camera exactly at the focal point of the telescope. The struts of the bench are placed in four slotted channels, which are fastened to the external payload housing structure. This permits the housing to expand and contract relative to the optical bench. Aerodynamic heating of the payload housing causes it to expand during flight. However, since the optical bench is fastened to the housing only at one point forward end), the focal length relationship between the mirror and camera is maintained.

2.2.3 Payload Housing

Figure 2-3 shows the payload housing. It is made from 1/8-thick 6061-T6 Al. and is 82 inches long. Two large areas are cut out which allow for installation and access of instrumentation. Stiffener reinforcement around the cut-out area is provided in order to increase the bending stiffness of the structure.

2.3 X-RAY OPTICS

Incoming x-rays are reflected off the telescope surface at grazing incidence. The telescope has a Giacconi-Rossi mirror using confocal paraboloidal and hyperboloidal surfaces to image x-rays. Figure 2-4 shows the general characteristics of the x-ray telescope mirror and the overall optics design of the paylaod.

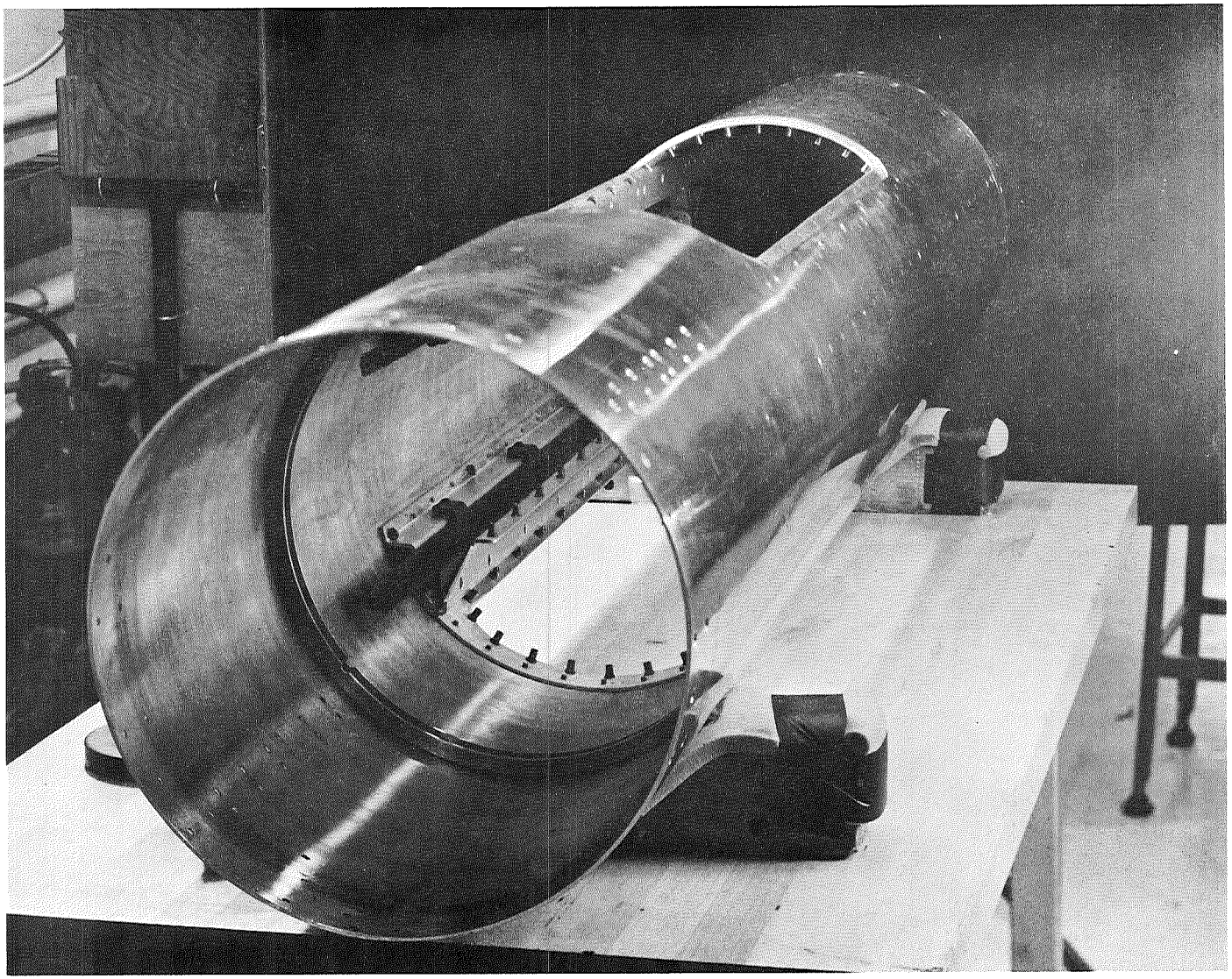

EG-002

Figure 2-3 Photograph of the payload housing.

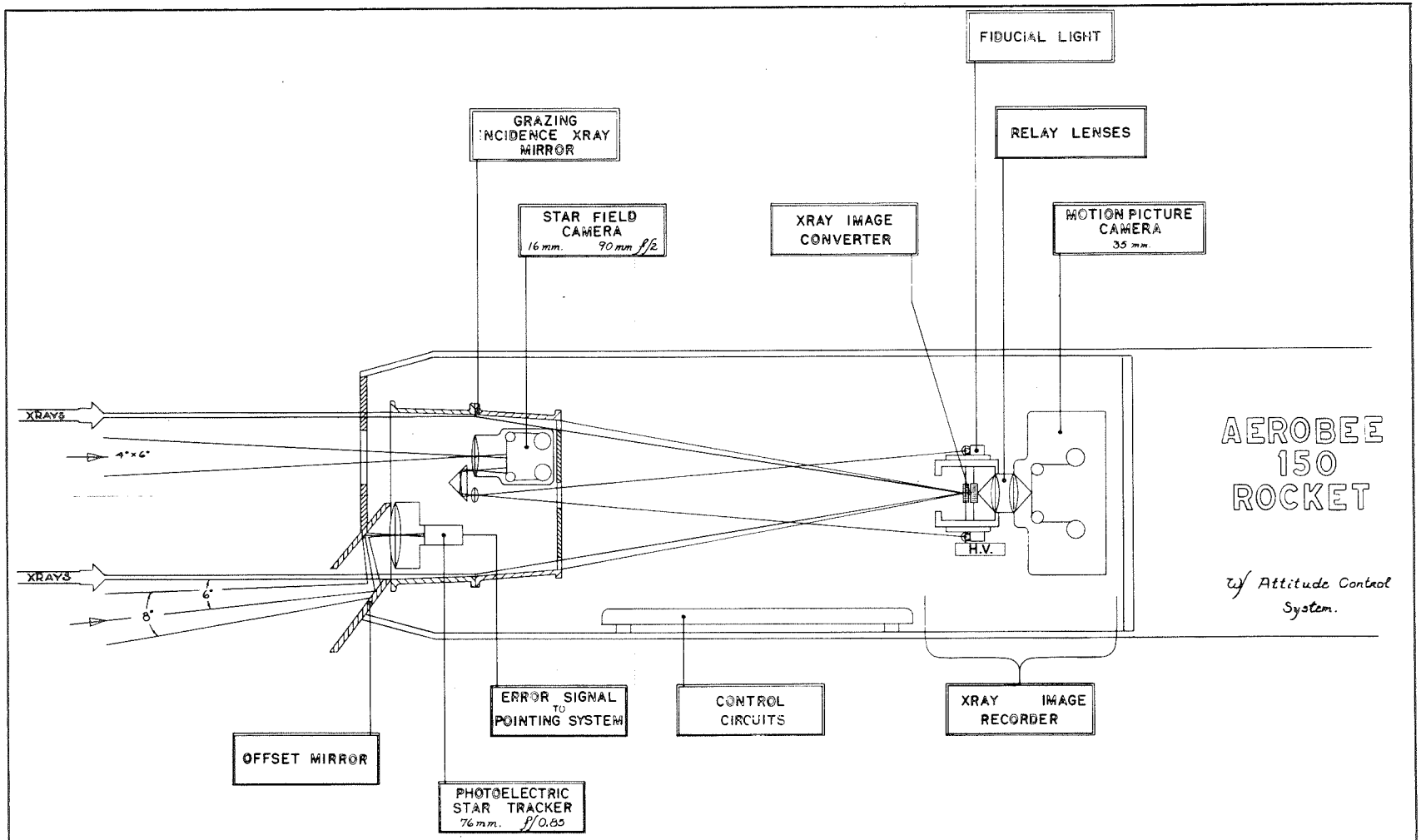

Figure 2-4 Schematic of the rocket x-ray telescope experiment.

The front portion of the mirror is configured to a paraboloidal surface whose 2-dimensional curvature is determined by the equation:

$$y^2 = 0.1865560\ (x + 104.00)$$

from $x = 4.500$ to $x = 0$.

The aft portion of the mirror is configured to a hyperboloidal surface whose curvature is described by the equation:

$$\frac{(x + 77.97668)^2}{672.3757} - \frac{y^2}{2.412200} = 1.0000$$

from $x = 0$ to $x = -4.500$.

Fabrication of the mirror requires precision machining and use of optical manufacturing techniques to obtain the desired surfaces; manufacturing tolerances for the mirror are as follows:

a. End faces flat within 0.0005 inch.

b. End faces normal to optical axis within 20 arc-sec.

c. Mirror surface concentric to optical axis within 0.0002 TIR.

d. Tolerance on the diameter of the mirror surface at the plane of intersection is $\pm$ 0.006 inch.

e. Diameters of the mirror surfaces of the two sections will match within 0.005 inch at the intersection.

f. Lateral misalignment of the paraboloid and hyperboloid at the plane of the intersection shall be no greater than 0.004 inch. Lateral play in the joint shall not exceed 0.002 inch.

The effective area of the telescope is 34 cm^2 and the approximate reflection efficiency is 4% for grazing angles between 0 and 1 degree.

Correlation of the x-ray telescope axes with the aspect camera axis was accomplished with a fiducial light system. A small light source is placed in the focal plane of the x-ray telescope. A ray from the fiducial light then leaves a collimating lens, mounted in

the mid-plane of the x-ray mirror at an angle corresponding to the fiducial light focal plane position. This ray is then reflected into the aspect sensor with a corner cube reflector and imaged along with the stellar field. The system effectively maps the x-ray focal plane onto the stellar field. Two such fiducial lights are necessary. Figure 2-5 is a schematic diagram of this system.

2.4 IMAGE RECORDING SYSTEM

The image recording system consists of a camera, an x-ray image intensifier and vacuum seal mechanism. Figure 2-6 shows a photograph of the assembled system, mounted in the rear of the payload. The vacuum door has been removed in this case, and replaced by a 1/8-in thick fused silica plate for use with ultraviolet light for boresight testing.

A 35mm Model 203-C-137 camera is used to record the x-ray counts; camera serial number is 1114 and is made by Giannini Scientific. The film transport is driven by a stepped motor and frame rate is adjustable by varying the drive circuit. A frame rate of 450 msec was used during the flight on 6 February 1970. The film used is Eastman Kodak No. 2485.

Figure 2-7 shows the vacuum seal mechanism for the image intensifier. A motor driven seal plate is used to seal and open the entrance aperture of the image intensifier. A mechanical toggle action against the seal plate is used to compress a viton o-ring seal.

2.5 ASPECT OPTICS

Exact pointing information is provided by the aspect system which records the star field in its 4^{o} x 6^{o} field of view.

The camera used is a Flight Research Model 3B and frame rate is 450 ms. Alignment of the aspect optics and x-ray optics is of primary importance and is performed in the laboratory using an optical bench; precision of this parallel alignment is several arc-seconds.

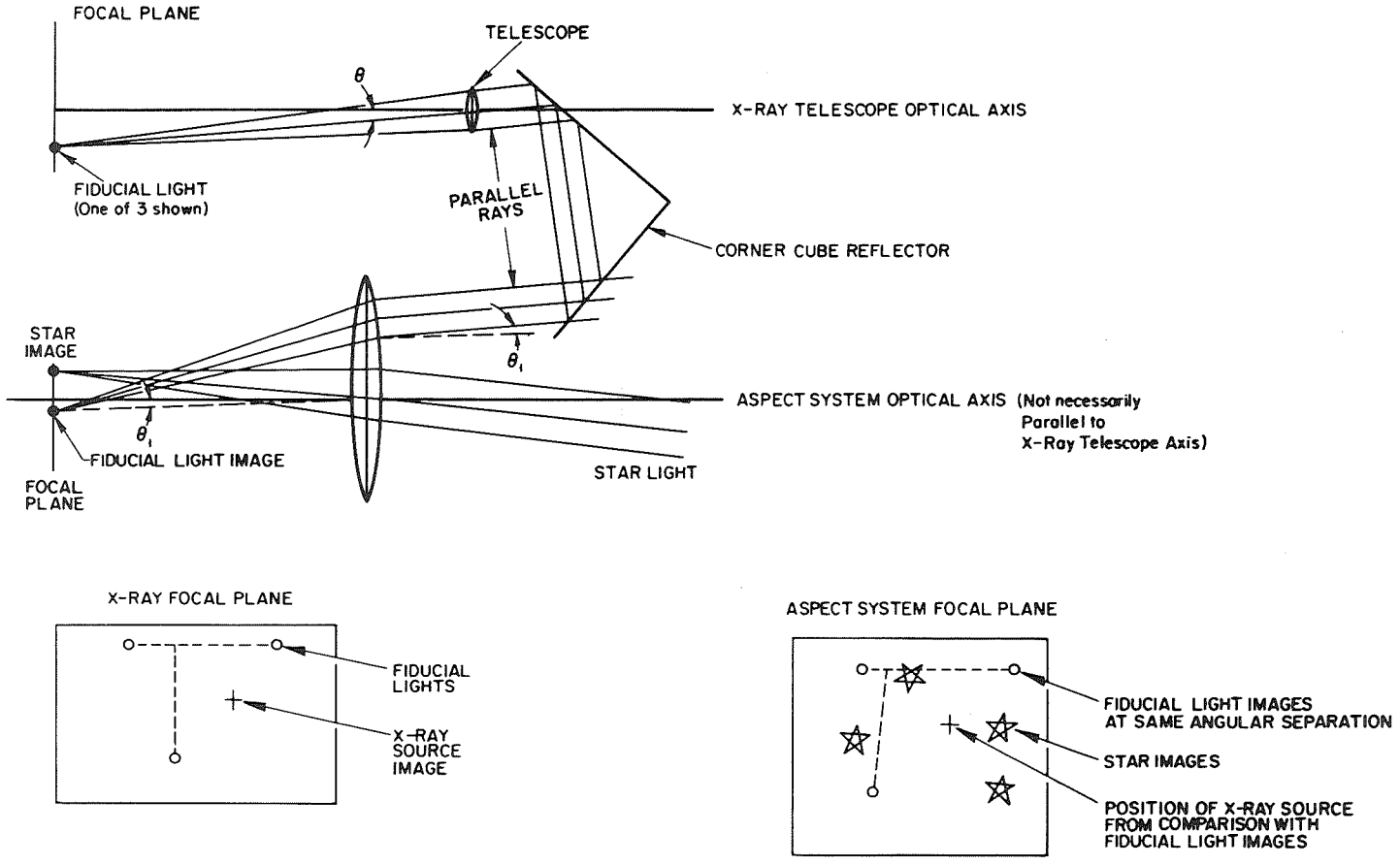

Figure 2-5 Aspect System optical concept including the technique used to correlate the x-ray telescope focal plane positions with the aspect system star field image.

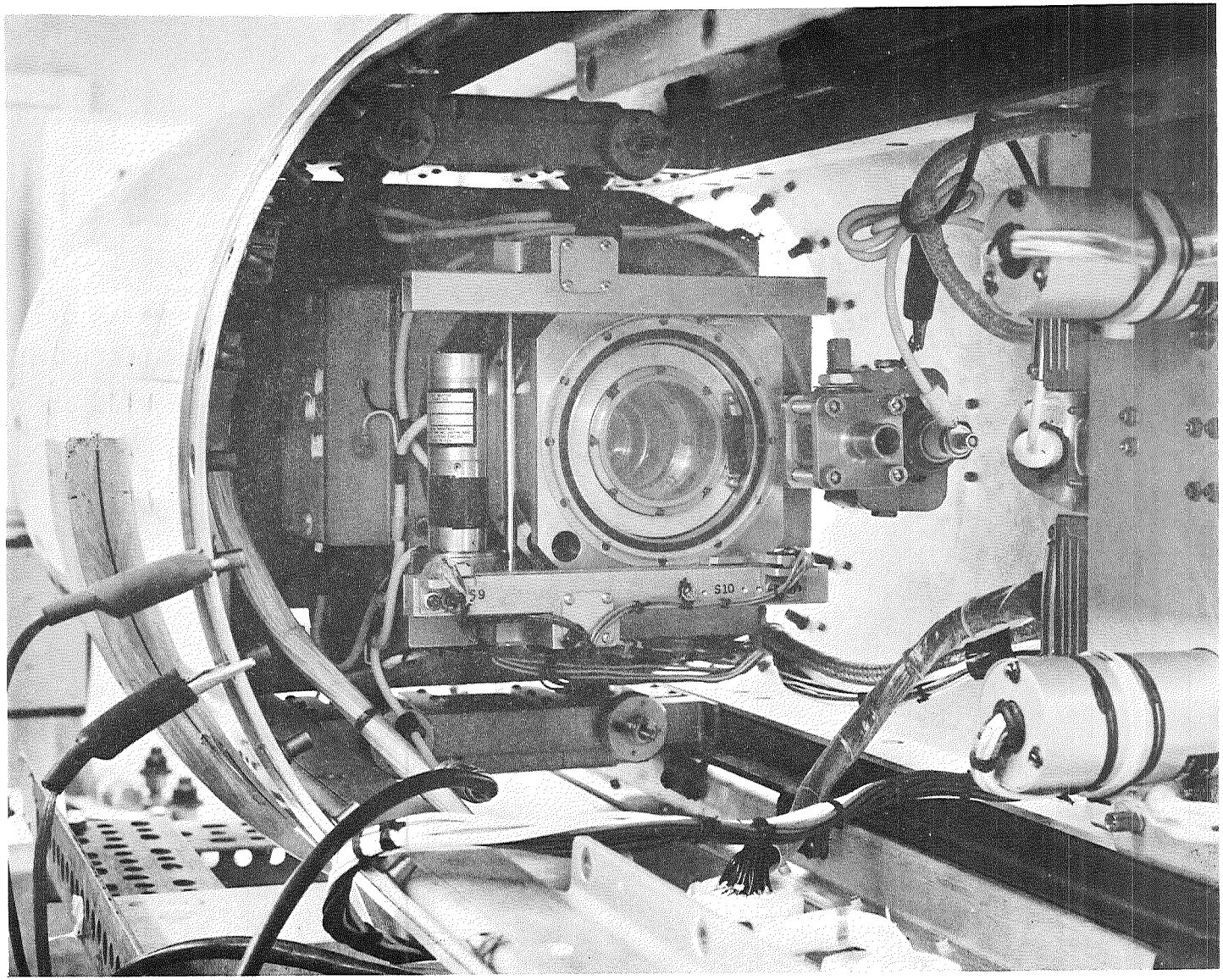

EG-011

Figure 2-6 Photograph of the image recording system.

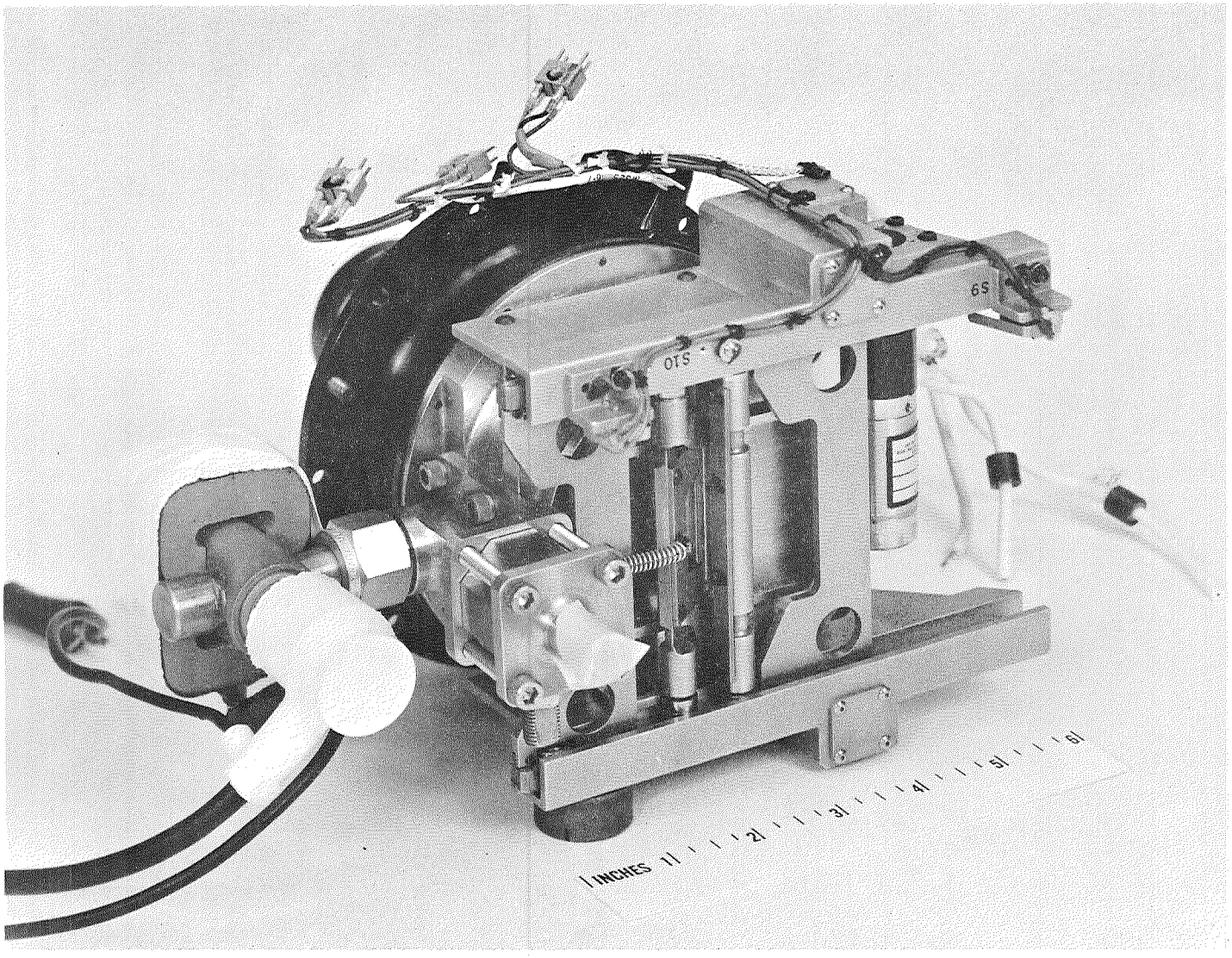

EL-001

Figure 2-7 The flight image intensifier vacuum chamber. The door in foreground will open at an altitude where the atmospheric pressure is about one micron. The ion pump is at the left, and the relay lens is partly visible to the rear.

Projected fiducial lights are used on the aspect film which provide a reference coordinate system for the star field, with respect to the x-ray telescope axis.

2.6 FINE POINTING SENSOR

It is necessary to point the x-ray axis of the payload to predetermined stellar targets. Ideally, it is desirable to have perfect pointing control with no errors, however, practical limitations in the attitude control system result in a limit cycle in the order of 10 to 30 arc-seconds. A photo-optical device is used, termed Fine Guidance Error Sensor (FGES), to view a specific portion of the star field. The instrument was the Model III, Serial No. 20, which is manufactured by ITT Aerospace/Optical Division, San Fernando, California and was supplied GFE by NASA. Figure 2-8 shows the instrument which contains a lens system, photomultiplier and power supplies. The tracker provides star position information in two axes mutually perpendicular to the boresight axis. Its mode of operation is to scan a large square field of view ($\pm 4^{o}$), select the brightest star and switch to a smaller field of view ($\pm 1/4^{o}$) centered about the acquired star. Pitch and yaw error signals are produced as the star position varies from the center-null position. These signals are amplified and used to actuate the attitude control system which applies pitch and yaw corrective maneuvers to maintain the acquired star at the null-position.

The FGES is designed for night-time use and must not be exposed to daylight or bright light sources when power is applied.

Since the portion of sky of scientific interest with respect to x-ray studies did not contain bright stars, the tracking axis was shifted six degrees in order to view bright stars. The tracker requires zero to third visual magnitude stars for proper operation. Two mirrors were used to provide the offset tracking as shown in Figure 2-4.

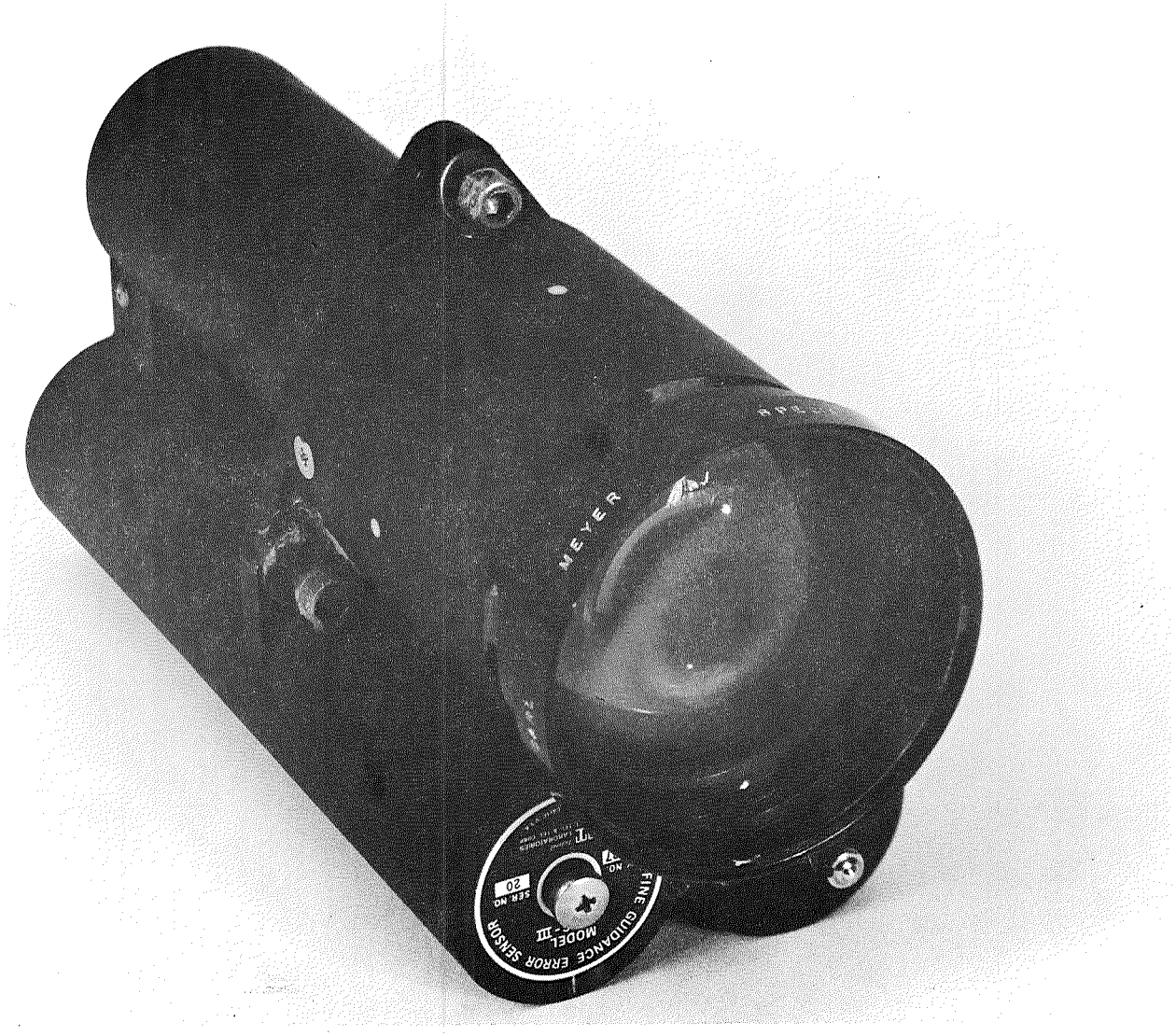

EG-015

Figure 2-8 Photograph of the Fine Guidance Error Sensor.

A 3-degree skew angle between the mirrors provides the 6-degree offset. These mirrors were pyrex substrate vapor-coated with aluminum, polished and overcoated with a special film to provide scratch resistance. Reflectivity at 4200 Å was intended to be 90%, however, only 80% was achieved. Since there is a double reflection of the starlight before it enters the FGES, it is important to obtain as high a reflectivity as possible from these mirror surfaces.

2.7 PAYLOAD ELECTRICAL SYSTEM

The electrical system of the payload is composed of (a) timing circuits, (b) power control and switching, (c) monitor circuits, (d) camera control, (e) pyrotechnic circuits, (f) batteries, (g) image intensifier control, (h) payload controls, (i) commutator, and (j) telemetry. Figure 2-9 shows the overall design of the electrical system and Figure 2-10 shows the main electronics panel. External to the payload a control console is used to provide operation of the payload.

2.7.1 Timing Sequence

Sixteen functions are performed in-flight for proper operation of the experiment. Prime commands for the experiment are received either from timers in the telemetry instrument package or the ACS system. Timer switch closures are also provided by AS&E timing circuits which are located on the main electronics panel.

The in-flight control functions are as follows:

	Event	Time from Lift-Off
		(sec)
1.	Lockout OFF High Voltage Power Supply ON	52
2.	Coast	52
3.	Start despin and erect	67
4.	Eject nose cone	72
5.	Back-up nose cone eject	77

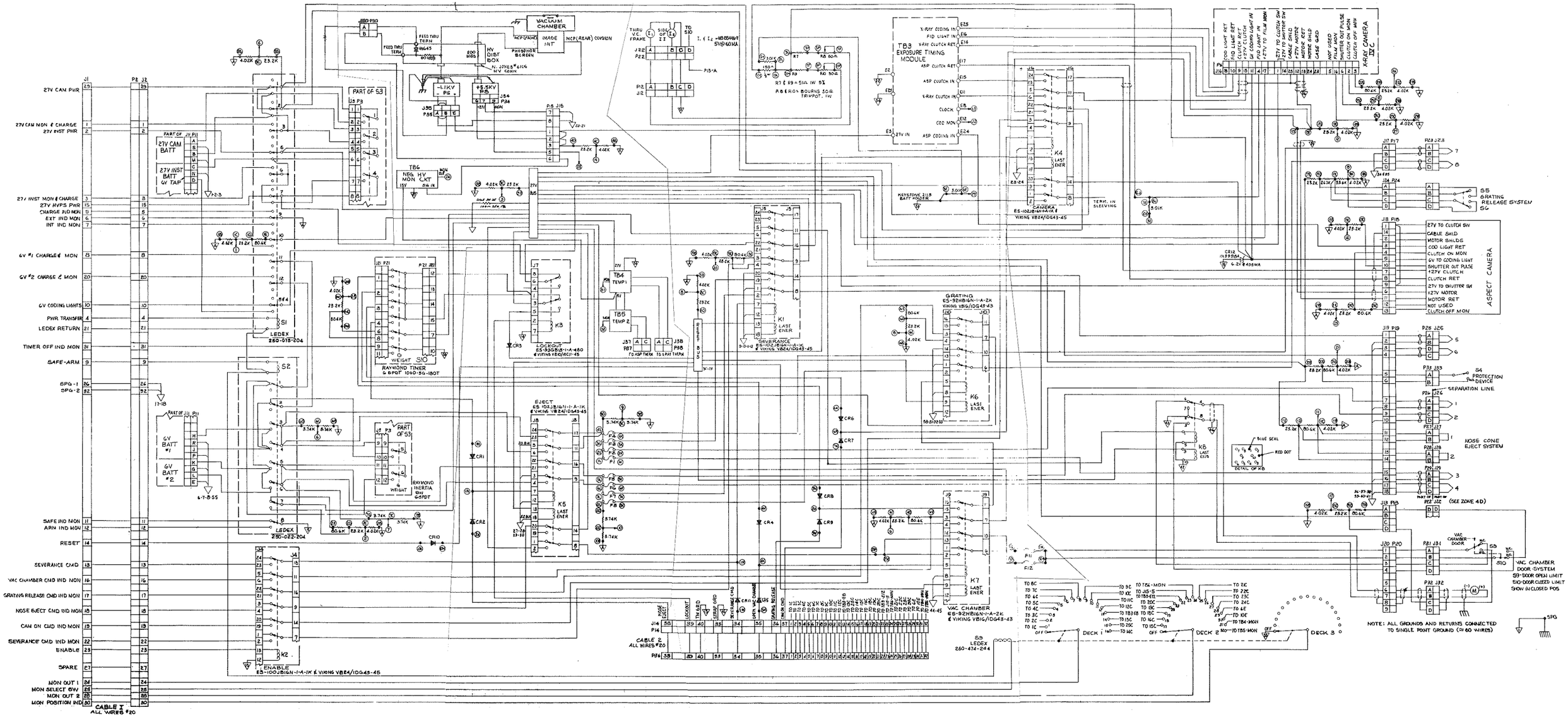

Figure 2-9 Wiring diagram for the Stellar Telescope Rocket.

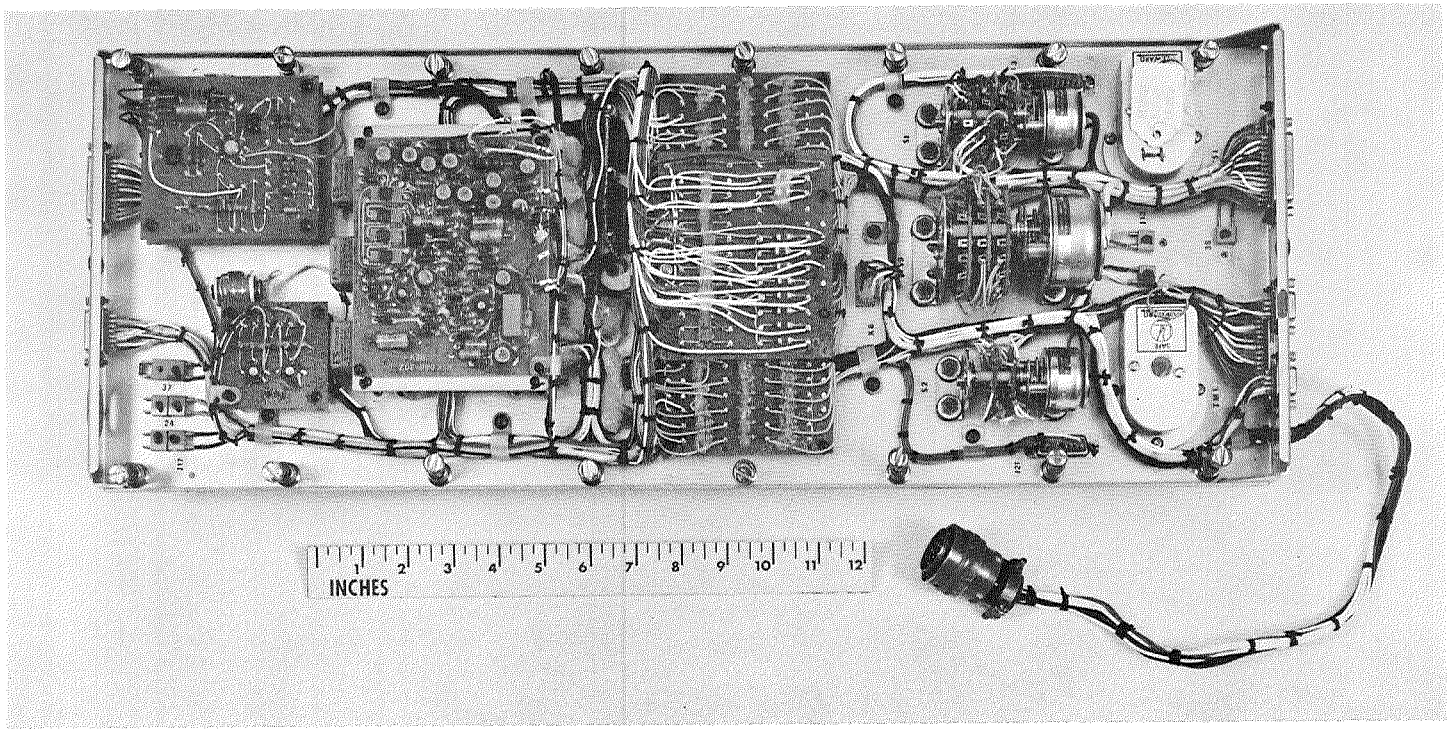

EG-006

Figure 2-10 Photograph of the main electronics panel.

6.	Stabilize (2 sec)	82-97*
7.	Remote Adjust. (6 sec)	84-99
8.	Start Cameras	84-99
9.	Back-up Camera Signal	99
10.	Start First Maneuver	90-105
11.	Open Vacuum Door	90-105
12.	Back-up Vacuum Door Open	105
13.	Close Vacuum Door	350
14.	Close Mirror Protector	350
15.	Shut-off High Voltage Power Supply	350
16.	Payload Separation	350

*Event will start sometime during this period. The start despin and erect period can vary from 15 to 30 seconds thereby causing a 15 second uncertainty in the actuation of subsequent events as indicated.

All the timer commands operate through multi-pole latching relays except for the lockout function. One coil on each relay is tied to a common reset which is energized by lockout or externally from the control console. The multiple inputs to the control coils of each relay are electrically isolated by diodes.

2.7.2 Camera Control

Both the x-ray recording camera and aspect camera film transport mechanism are driven by clutch-brake motor combinations. The electronics panel contains the circuit module which provides the timing, pulse shaping and driving circuits for the motors. Both cameras are operated at a frame rate of 450 milliseconds. In conjunction with the pulsing of the camera motors, the circuit module also actuates two small light bulbs which provide fiducial marks on the aspect film. Also a coding light for each camera is actuated

every eighth frame. The timing module operates whenever power is turned on, however, the cameras and light operate through the start camera command.

2.7.3 Image Intensifier Control

Two high voltage power supplies, a high voltage distribution box and an ion pump are required to operate the image intensifier assembly. The ion pump is used to maintain a proper vacuum condition (in the order of 0.1 micron) in the chamber. A separate umbilical was used to operate the ion pump which could be operated up until launch.

2.7.4 Pyrotechnic Circuits

Two pyrotechnic circuits are provided in the scientific portion of the payload. The ejectable nose cone and mirror protection cover are actuated by Model 2801 Holex guillotine cutters which are electrically initiated. Figure 2-11 shows the electrical circuit which is used for firing the devices. The system uses redundant bridgewires in each guillotine cutter, and redundant timing and batteries. An arming switch is closed before launch and the safety pin is manually extracted from the Raymond timer thereby arming the circuit. As an additional safety precaution a lockout relay is provided which prevents the command relays from firing the guillotines until the lockout timer command actuates the lockout relay. This represents an in-flight arming function. Also the bridgewires are shorted and held at ground potential until actuation. The circuit conforms to range safety requirements.

2.7.5 Commutator

Experiment monitor data are obtained as a commutated data channel. A 29 segment, 2.5 RPS, Model 951-4 Datametrics commutator is used. Data segments are as follows:

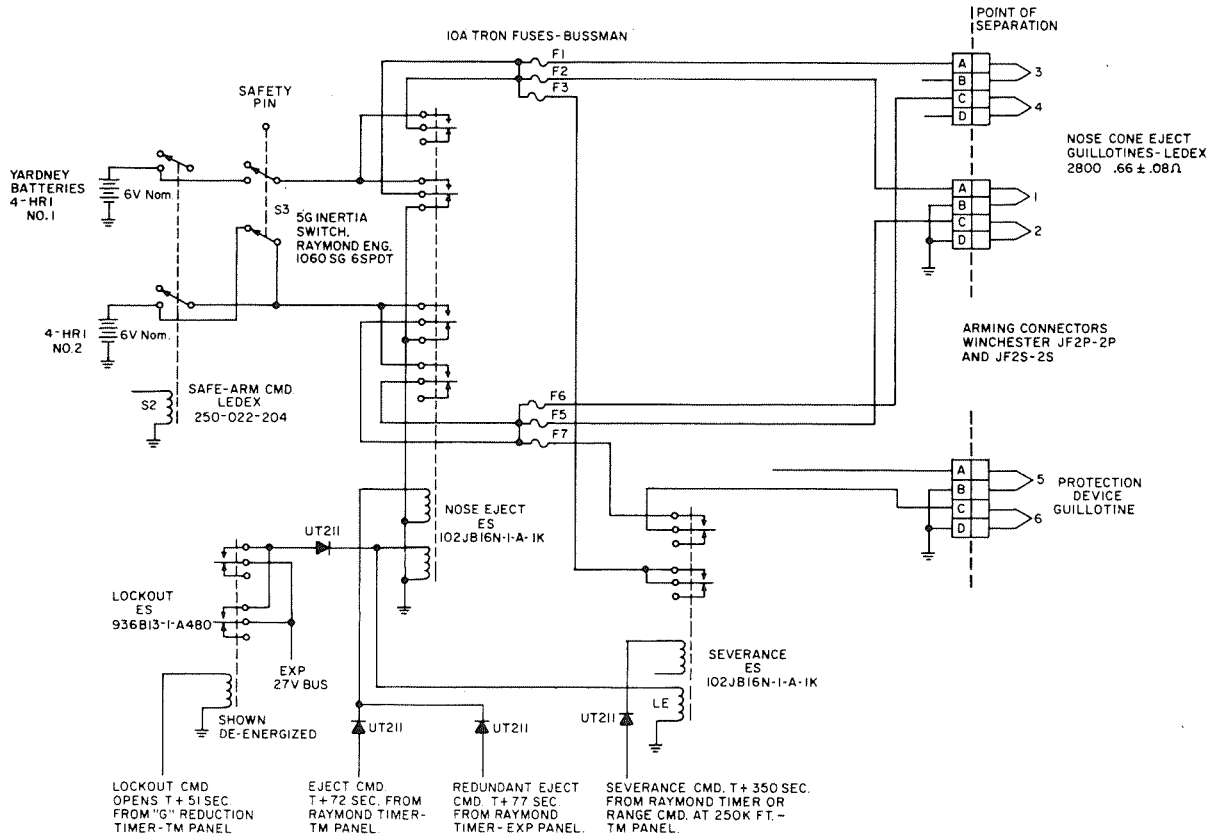

Figure 2-11 Schematic of the stellar rocket squib circuits.

Segment	Data
1	Ground
2	External - Internal Monitor
3	Safe - Arm Monitor
4	27V Inst. On
5	27V HVPS On
6	27V Camera On
7	6V #1 On
8	6V #2 On
9	Lockout Relay Monitor
10	6V #1 Eject Command
11	6V #2 Eject Command
12	Nose Cone Monitor
13	Camera - On Command
14	Vac. Chamber Command
15	Vac. Chamber Door Monitor
16	Grating Command
17	Grating Monitor
18	Severance Command
19	Protection Device Monitor
20	5.1 KV P. S. Monitor
21	1.1 KV P. S. Monitor
22	Aspect Camera Clutch Monitor
23	Timer Position Monitor
24	Fiducial Light Battery Monitor
25	Fiducial Light Monitor
26	X-ray Temp. Monitor
27	Aspect Temp. Monitor
28	Spare
29	Sym. Pulse 5V

2.7.6 Telemetry

The telemetry system is furnished GFE and serviced by NASA personnel. The telemetry instrumentation panel is located in the experiment section of the payload. A pulse position modulation (PPM) telemetry system is used with a 10K Hz sampling rate. Fifteen telemetry channels are used on the experiment and attitude control system as follows:

Channel	Data
2	PC/Yaw valve
3	Experiment Commutator
4	Roll valve/output pulse
5	Pitch Gyro Tracker Hi-gain
6	Yaw Gyro Tracker Hi-gain
7	Tracker Pitch Low - gain
8	Roll Position Tracker Yaw Low - gain
9	Clock
10	Aspect Cam Shutter Pulse
11	X-ray Cam Shutter Pulse
12	Coding Light
13	X-ray Clutch
14	X-ray Film
15	ACS & Vehicle Commutator
16	Accel/Pitch Valve

Data transmission occurs in real time.

2.7.7 Ground Support Equipment

Support equipment which is used to externally control the experiment portion of the payload consists of a control console, which is shown in Figure 2-12, and a power supply for operating the ion pump. The main umbilical cable contains 31 wires and uses a FK-L32-21C9/16 connection which mates with a FKP-L32-32SL connector in the payload.

EG-014

Figure 2-12 Photograph of the GSE control console.

The control console allows testing alignment, and calibration of the scientific payload through the umbilical cable. It enables the system to operate on external power supplies and switch to the internal battery supply. Timer commands are simulated to actuate the various functions which occur in-flight. Analog readout of monitors and certain data channels are displayed on the control console. Prior to launch the payload system engineer uses the control unit to arm the payload, switch to internal power, and monitor the command function to assure they are in the "safe" position.

3.0 PREFLIGHT TESTING AND EVALUATION

3.1 IMAGE INTENSIFIER EVALUATION

Two parameters affecting the performance of the image intensifier are the voltage across the microchannel plate and the phosphor potential. A testing program was carried out in which the two parameters were varied while film records were made of the image intensifiers' response to x-rays. Increasing either voltage increases the efficiency of the device, until a plateau region is reached. Use of too high a voltage across the microchannel plate degrades the resolution because at the resulting high gains enough light is generated by the phosphor to produce halation in the film. The image intensifier in flight was operated near the low voltage end of the plateau, where halation was not a problem.

[The quantum efficiency for 8.3 Å x-rays was measured as 6% with 1100 volts across the microchannel plate and a screen potential of 4900 volts; these are the values used in flight. The size of a typical spot on the film was about 60 μ M, corresponding to a resolution of 8 line pairs/mm, or about 20 arc seconds for our x-ray telescope. But in fact the spot center could be located with uncertainty much less than the spot diameter, so the experimental resolution was limited by the telescope rather than the image intensifier. Our background rate at this time was about 1/sec and was reduced very substantially when later tested in the ion-pumped flight chamber.]

An attempt was made to improve the efficiency by depositing a thin layer of MgF_2, a photoelectric material, on the face of the microchannel plate. Subsequent measurements of the efficiency as a function of position on the image intensifier gave the result shown in Figure 3-1. No effect attributable to the deposition is seen when the image intensifier is operated in the plateau region. The decrease

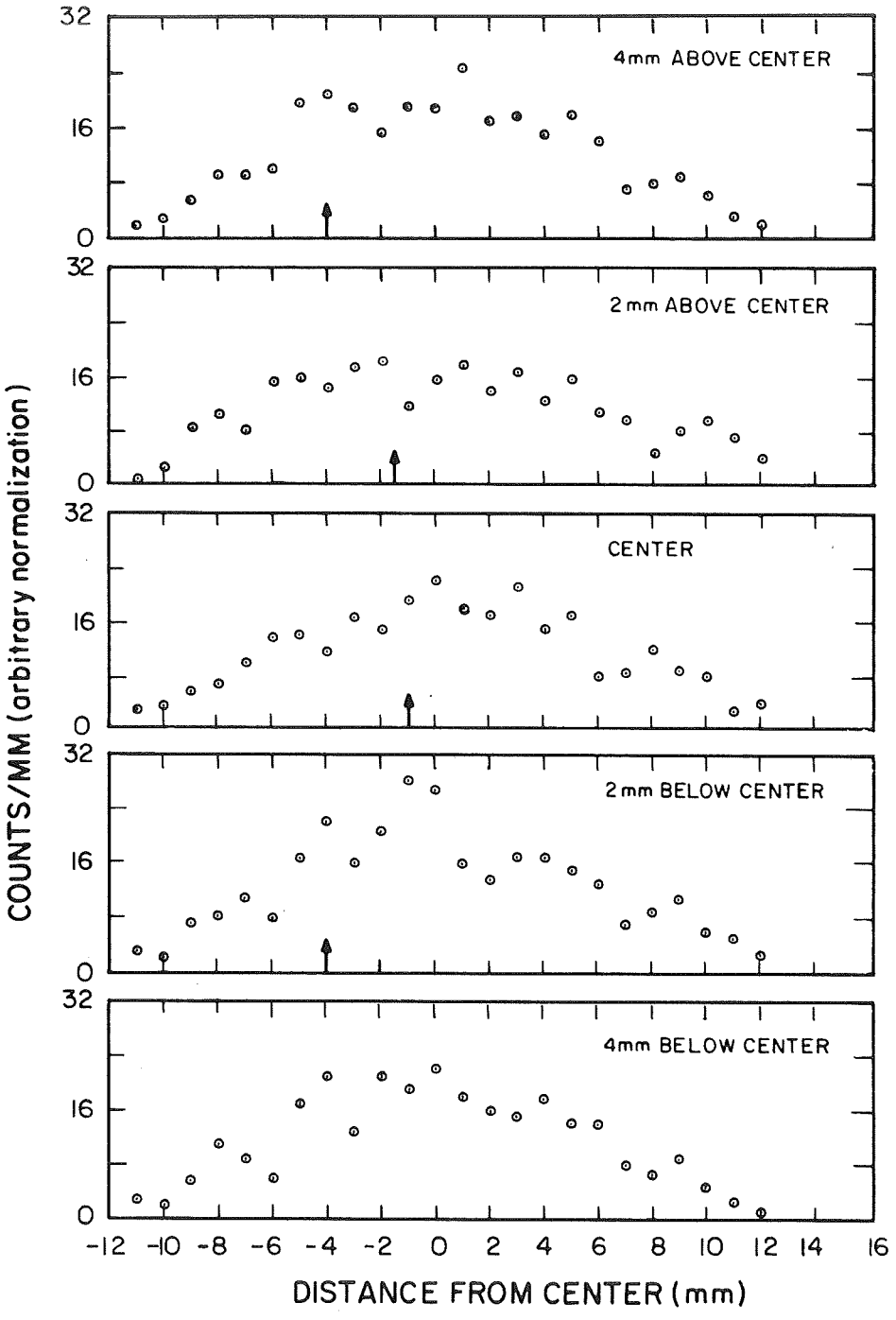

Figure 3-1 Efficiency as a function of position on the image intensifier.

in efficiency near the edge results from geometrical vignetting in the relay lens system. The central region of relatively high quantum efficiency corresponds to a field of view of about 35 arc seconds in our telescope.

3.2 ALIGNMENT OF OPTICS

Several of the alignment procedures required a collimated light beam, which was produced by placing an illuminated pinhole in the focal plane of a parabolic mirror. Figure 3-2 shows the pinhole, with divergent light shining through the opening in an annular optical flat. Nearly collimated light from the parabolic mirror is reflected from the flat and refocussed by the parabolic mirror. If the focus is in the plane of the pinhole, as measured by the Foucault knife-edge test, the pinhole is in the focal plane of the parabolic mirror.

The x-ray telescope is provided with an optically flat surface normal to its optic axis. Figure 3-3 illustrates the procedure for aligning this surface normal to the collimated beam. The beam strikes a partially reflecting glass flat. The reflected portion is turned just 180° by a cube corner prism, partly transmitted through the glass, and viewed by a theodolite. The part of the collimated beam originally transmitted through the glass flat is reflected successively by the telescope flat and the glass flat, and viewed by the theodolite. When the two beams enter the theodolite parallel, the telescope is aligned to the beam.

Boresighting of the startracker was then effected by setting the tracker error signal to zero with the same beam in its field of view. In order to set the offset mirrors so the tracker looks at a pointing star 6° 51' from the telescope axis, the theodolite was used to set up an autocollimator so its beam made that angle with the beam from the parabolic mirror, as shown in Figure 3-4. The telescope was

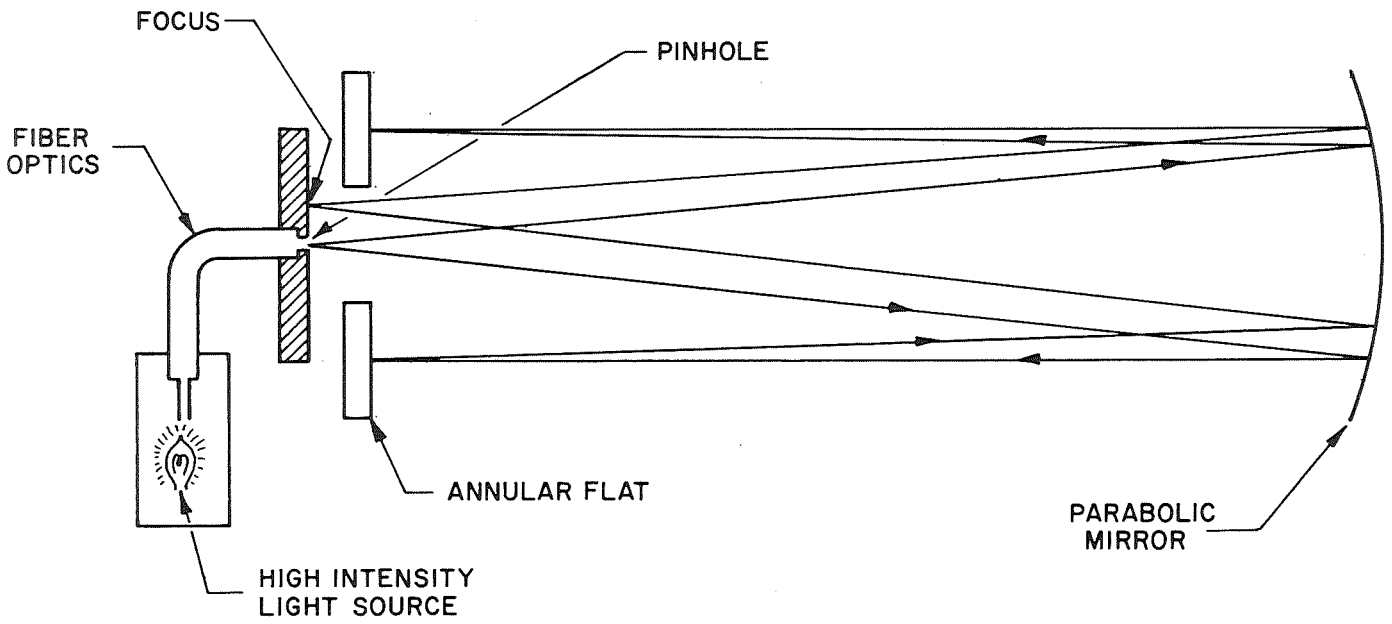

Figure 3-2 Schematic diagram of the system to produce a collimated light beam for alignment purposes.

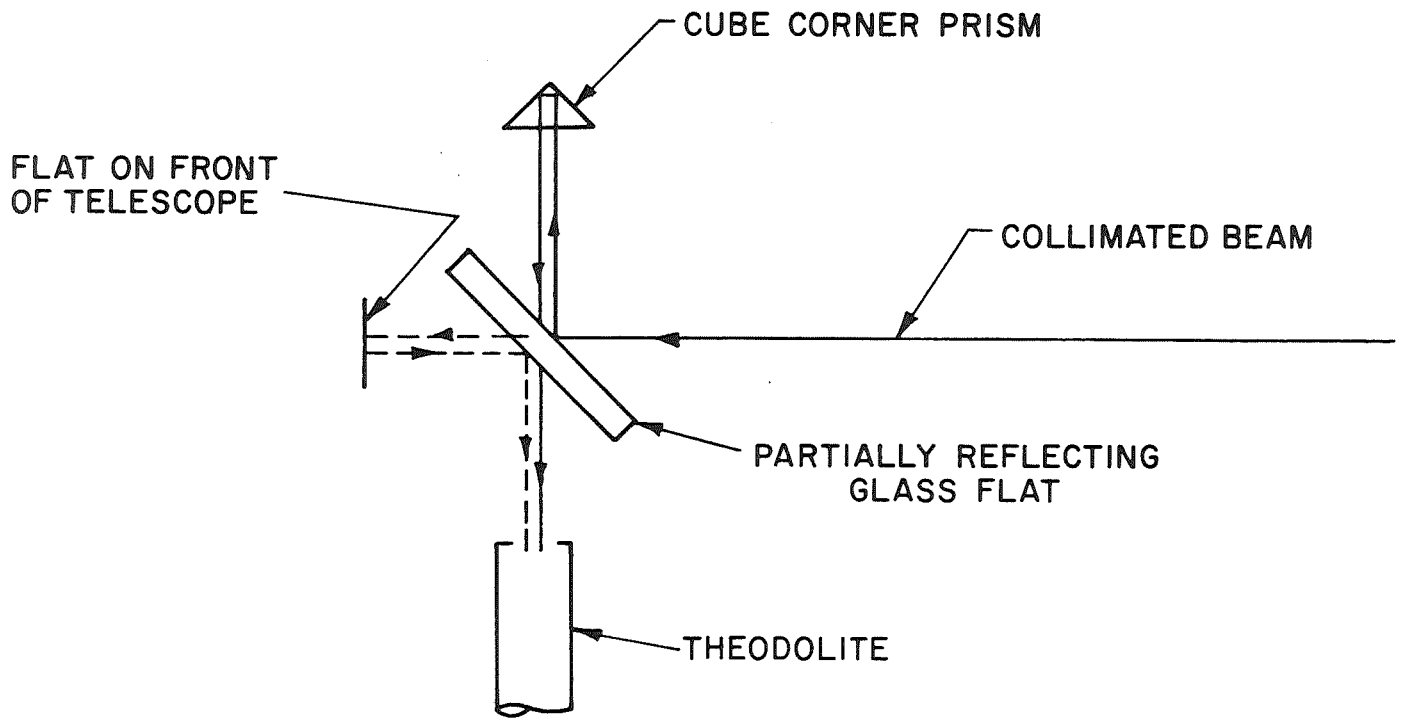

Figure 3-3 A schematic diagram of the optical set up to align the telescope to the collimated beam.

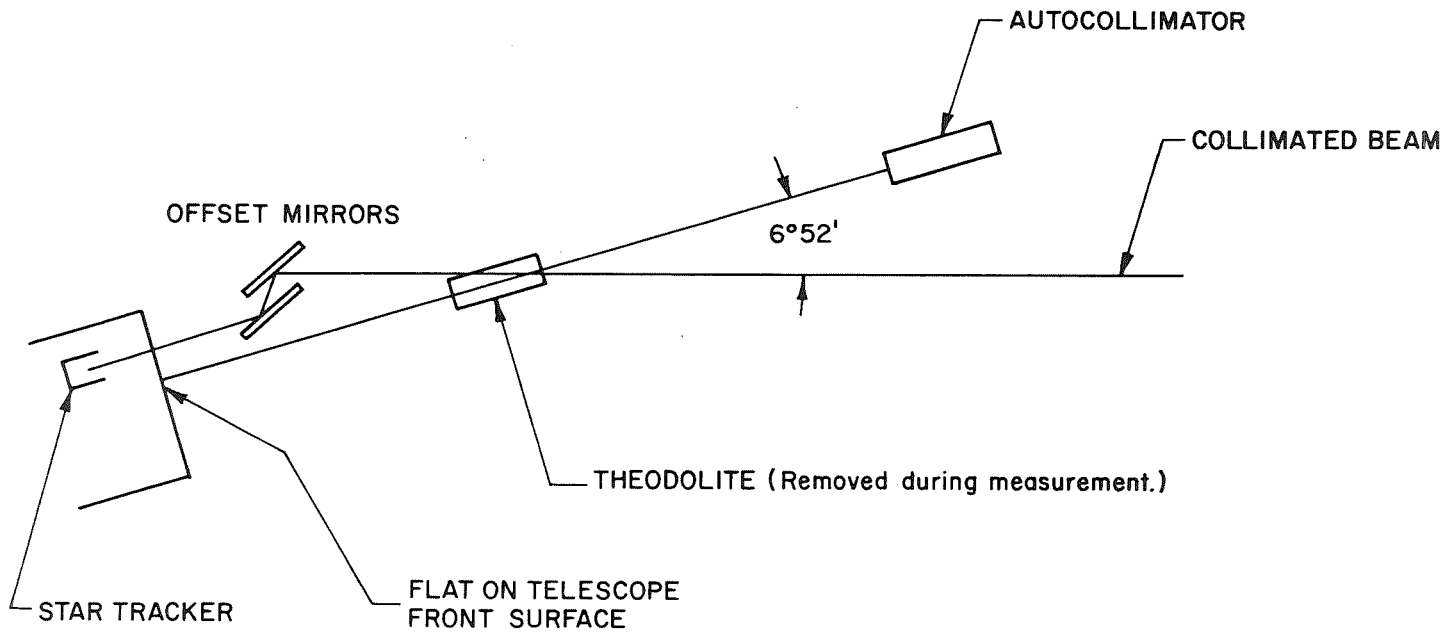

Figure 3-4 A layout of the optical set up used to boresight the star tracker.

aligned parallel to the autocollimator beam. Then the offset mirrors were installed, and adjusted until the tracker error signal was zero with the tracker viewing the parabolic mirror through the offset mirrors.

Focussing of the x-ray mirror, which meant placing the front face of the microchannel plate in the focal plane, was checked by two independent techniques. In the first, illustrated in Figure 3-5, a flat mirror was placed near the focal plane, and the telescope was aligned to the collimated beam. If the flat mirror is precisely in the telescope focal plane, the reflected light will return through the optical system and refocus in the plane of the optics. (In fact a small flat mirror was used to bend the optical path and bring this focus out to the side where it could be observed without interference with the rest of the optical path. The position of this focus was determined relative to a similar focus with a flat mirror in front of the telescope mirror). If the second focus is displaced from the reference plane by an amount a_1, the displacement a_2 of the flat mirror from the focal plane is given approximately by

$$a_2 = \left(\frac{F_2}{F_1}\right)^2 a_1$$

where F_1 and F_2 are the focal lengths of the parabolic mirror and telescope mirror respectively. The approximation is good for small a_1, a_2, and indicates the distance the flat mirror should be moved to give the next approximation to focus. As focus was approached, the Foucault knife-edge test became quite insensitive, so that the final focus could not be verified by this technique. As a check, pieces of photographic paper were mounted on the flat mirror and exposed in the collimated beam, with the flat mirror in various positions near the focal plane. Examination of the resulting images verified the original focus within . 002 inches.

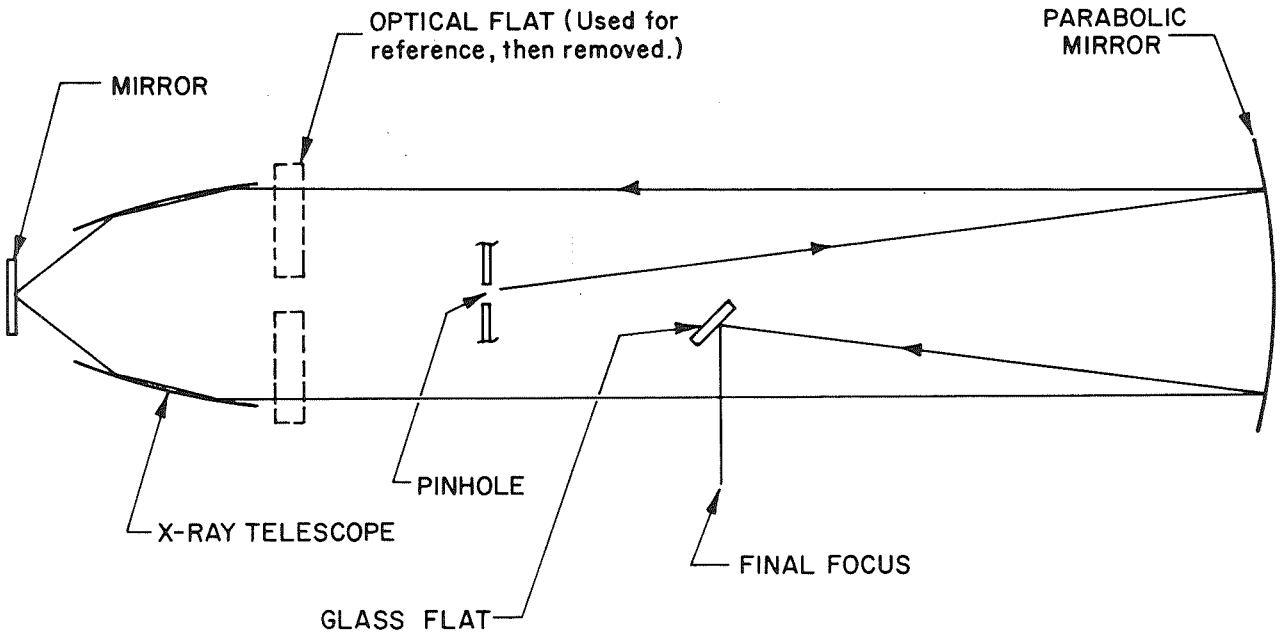

Figure 3-5 A layout of the experimental set up used to focus the x-ray mirror.

Both the 16 mm camera used for aspect and the 35 mm used for recording the output of the image intensifier were focussed on infinity. In each case, collimated light was shone on the camera, and photographs taken for various lens positions. Examination of the resulting images allowed determination of the correct position. The relay lens was focussed by placing it in its mount viewing the fiber optic output of the image intensifier. A telescope focussed at infinity was used to view the image intensifier through the relay lens, and the relay lens was adjusted for best image.

A collimated ultraviolet light beam was used to boresight the aspect camera relative to the x-ray telescope. The door of the flight vacuum chamber was replaced by a quartz flat, which transmitted enough ultraviolet to be detected by the image intensifier. The source emitted visible light as well as ultraviolet. Both the x-ray telescope and the aspect camera viewed the beam, and exposures were taken with the 16 mm and 35 mm cameras. Measurements on the resulting films resulted in telescope-aspect boresighting with an uncertainty of about 20 arc seconds. We feel confident that this boresight technique can yield much more precise results with some further development.

3.3 SYSTEM TESTS

The most important system elements include the image intensifier, vacuum chamber door, ion pump, 16 mm and 35 mm cameras, and power supplies. The system was tested in a large tank which could be evacuated to 10^{-5} Torr. X rays were supplied by a bremsstrahlung generator 60 feet from the front face of the telescope, and by an Fe^{55} source outside the chamber door. Before the test, the ion pump was holding the pressure in the chamber below 10^{-5} Torr. Since the ion pump was not to be operated in flight, power was supplied to it through an unpotted connector;

Figure 3-6 Photograph from the system test showing focussed x-rays and diffuse background.

consequently, as the tank was roughed down through the corona region the ion pump power supply was turned off. When the tank vacuum reached a few times 10^{-4} Torr the supply was turned back on and the ion pump started after some delay. The cameras and image intensifier were turned on, and the vacuum chamber door was opened. The bremsstrahlung generator was operated part of the time. After the chamber door was closed and the tank returned to atmospheric pressure, the ion pump was again started with some delay.

The developed films showed that both cameras operated properly. The image intensifier responded to the diffuse Fe^{55} x rays and the focussed bremsstrahlung as shown in Figure 3-6. The focus, however, could not be checked by this technique because the source was not at infinity. The relay lens - 35 mm camera lens system was in focus. Monitor readings indicated that the image intensifier power supplies produced the design voltages.

3.4 INTEGRATION TESTS

Integration and Environmental Testing was performed at GSFC on December 15 through 19, 1969.

On December 17th, the payload was turned on. The high voltage supply output voltages were checked, while disconnected from the image intensifier. The screen read 4900V and the NCP read -1080, satisfactory. At 1:30 p. m. the integration test was run while the payload was mated to ACS and T/M. All instruments functioned properly in the payload.

Later on the 17th, a bend test was performed. Under torques of about 45, 000 in-lb the payload deflected 1/16 inch or less, satisfactory.

On the 18th, a pre-shake alignment check was run. The boresighting between the star tracker optic axis and the x-ray telescope axis was checked, using the procedure described in Section 3.2. At this time, the boresighting could be checked to a precision of 8 arc min., which was adequate, but was to be improved upon later.

Late in the afternoon of the 18th, the payload was moved to the T & E building in preparation for the vibration test, which was conducted the next morning. The payload structure survived the shake with no damage. The image intensifier ion pump could not be run during the shake, since it was powered externally through an umbilical cord, which was not connected during the test. However, it was connected up after the test and the ion pump re-started, indicating that no substantial loss of vacuum had occurred. Later events suggest that it would have been desirable to monitor ion pump current during the test, and to shake the image intensifier chamber in a vacuum ambient to remove the extra door closing force exerted by the atmosphere on the seal.

At 3:30 p. m. on December 19th, another integration test was run, successfully. The payload was shipped back to AS&E that day.

3.5 POST-INTEGRATION TESTS AT AS&E

On December 24th, the star tracker offset mirror alignment was checked and was found to be the same as prior to the vibration test within 2 arc min. This was satisfactory.

The alignment of the star tracker optic axis to the x-ray telescope was checked also that day. A defect was found in one of the optic elements, which had been giving false alignment shifts of about 5 arc minutes. An improved optic system was adopted and with it, we established that the tracker-to-telescope alignment had

shifted 8 arc minutes or less. It was clear that most of the nominal shift of 8' had come from the defect in measurement mentioned above. The precision of the new technique was measured to be about $\pm$ 20 arc seconds by comparing several alignment measuring techniques for internally consistent results.

4.0 OBSERVING PROGRAM FOR FLIGHT 4.262

The primary target was the Crab Nebula. It was decided to utilize the capability of the STRAP III system to observe a secondary target, IC 443 as well for a limited time.

Since neither of these targets is optically bright, we had to offset point from a bright star. The offset mirrors must be set for the correct angle, with an accuracy of 5 arc-min or better. The calculation of the angle X_{ij} between the Crab $(\alpha_i \ \delta_i)$ and the pointing star β Tau, (α_j, δ_j), is as follows:

$$\cos X_{ij} = \sin \delta_i \sin \delta_j + \cos \delta_i \cos \delta_j \cos (\alpha_i - \alpha_j)$$

$$X_{ij} = 6^{\circ}51'.5 \pm 1'$$

Assuming:

$$\alpha_i = 5^h \ 31.^m 5 \qquad \alpha_j = 5^h \ 23^m \ 7.8^s$$

$$\delta_i = +21^{\circ} \ 59' \qquad \delta_j = +28^{\circ} \ 34' \ 02''$$

This value was set into the offset mirrors. The ACS programmer was set to observe the Crab for 172 sec, and this was achieved in the flight (See Section 6).

The second target was IC 443, a supernova remnant suspected as a possible X-ray source based on phenomenological considerations. The offset data using γ Gem as the pointing star, are:

$$\alpha_i = 6^h \ 14.^m 64 \ 49.4^s \qquad \alpha_j = 6^h 34^m \ 49.4^s$$

$$\delta_i = +22^{\circ} \ 42'.8 \qquad \delta_j = +16^{\circ} \ 26' \ 37''$$

$$X_{ij} = 7^{\circ} \ 50'$$

The programmer was set to observe IC443 for 36.73 sec. IC443 is a supernova remnant of small radius which we suspected might be an x-ray source. Also, it is located near the Crab Nebula, and with an accessible offset pointing star, permitting its observation during the same flight as the Crab.

While the payload did not point stably to IC443, it did view the object for a few seconds.

5.0 LAUNCH AND FLIGHT REPORT

After shipment of the payload to White Sands, the setting of the offset mirrors was rechecked and found not to have shifted by more than one arc minute. The offset angle was set at 6° 50' 52", using the same technique as before.

The payload was moved outside on two successive nights in order to take star pictures. The tracker was able to lock onto stars, and the aspect camera recorded clear star images. In the absence of measuring equipment the offset angle could not be deduced accurately from these pictures, but a point 6° 51' from the pointing star was near the center of the aspect frame.

On returning the payload inside, a partial loss of vacuum was suffered each night; on the second night it was necessary to rough out the chamber in order to restart the ion pump. This effect was suspected to be due to thermal shock; the ambient temperature changed by about 30°F each time quite suddenly. The horizontal test was a run-through of the flight plan sequence. Certain functions, such as nose cone ejection and opening of the chamber door, could not be executed, but test lights came on as the commands were received. The experiment functioned normally. After installation in the tower, the payload went through the vertical test, another run-through of the flight plan, without difficulty.

The launch occurred at 8:00 PM on February 6, 1970. All systems operated and telemetry records indicated that all payload functions were normal, except that a monitor showed the microchannel plate voltage did not reach its design value until half way through the flight. The tracker acquired a star and held it for the part of the flight scheduled for observing the Crab. After the maneuver which

was to have pointed the telescope at IC 443, however, no pointing star was acquired.

Payload separation occurred on schedule and impact was on range. Recovery on the morning of February 7 was effected without difficulty. The payload was undamaged except for scratches and a small chip in one offset mirror, and minor scratches on the skin. When power was applied to the ion pump, it was found that air had entered and the pressure was above the corona region. This suggested that the door had not sealed completely when it reclosed upon severance (about 250,000 ft altitude) just before reentry, or perhaps that it had been jarred open when the payload struck the earth after descending on the parachute.

6.0 DEVELOPMENT OF FLIGHT FILM

The 16mm aspect film was found to contain star images of good quality. During the part of the flight when the tracker was locked onto a star, the aspect star field was stable and matched the field in the neighborhood of the Crab well enough that we are certain it pointed at the Crab (See Figure 6-1).

The 35mm camera was flown without a shutter. The first frame was severely blackened, indicating that the image intensifier flashed before the cameras started. A number of frames later in the flight were darkened. Most frames contained one or more spots which, because of the persistence and stability from frame to frame, were identified as image intensifier hot spots rather than scintillations due to x rays. One sequence of about twelve frames showed increasing numbers of scintillations until two frames which were substantially darkened, after which the number of scintillations receded. No spots related to any astronomical object were present (See Figure 6-2).

The failure of the image intensifier to reach its design voltage on schedule, coupled with the darkening of frames on the 35mm film, indicated that the flight chamber lost vacuum on ascent, leading to electrical breakdown in the image intensifier. When the door opened, it gradually pumped out, and the voltage came up. This was accompanied by ionization which caused the burst of scintillations described above. Apparently this series of events destroyed the image intensifier's sensitivity to x rays, so no x rays from the Crab Nebula were observed.

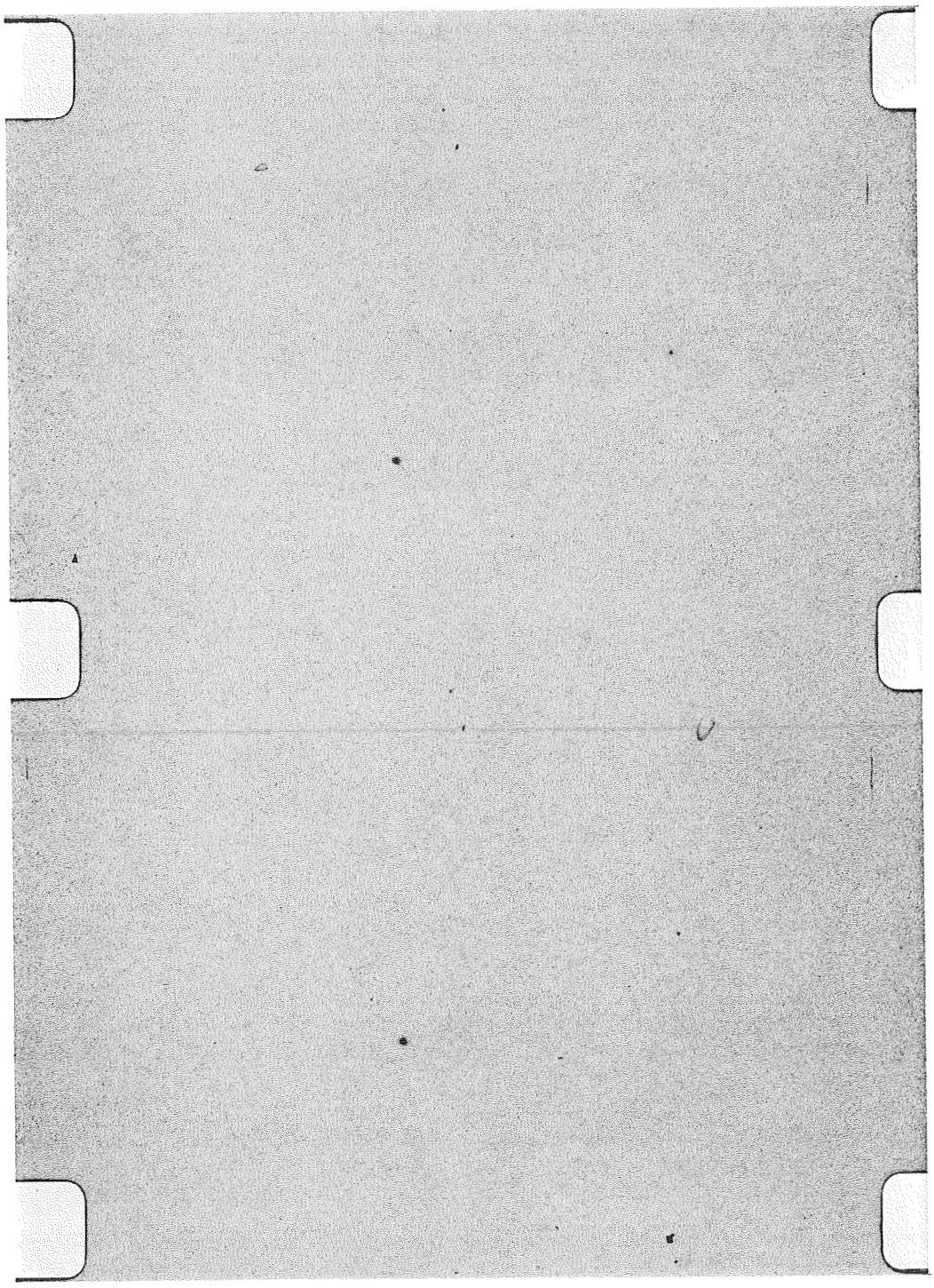

Figure 6-1 Two frames from the flight aspect film showing the star field in the neighborhood of the Crab Nebula together with the fiducial lights.

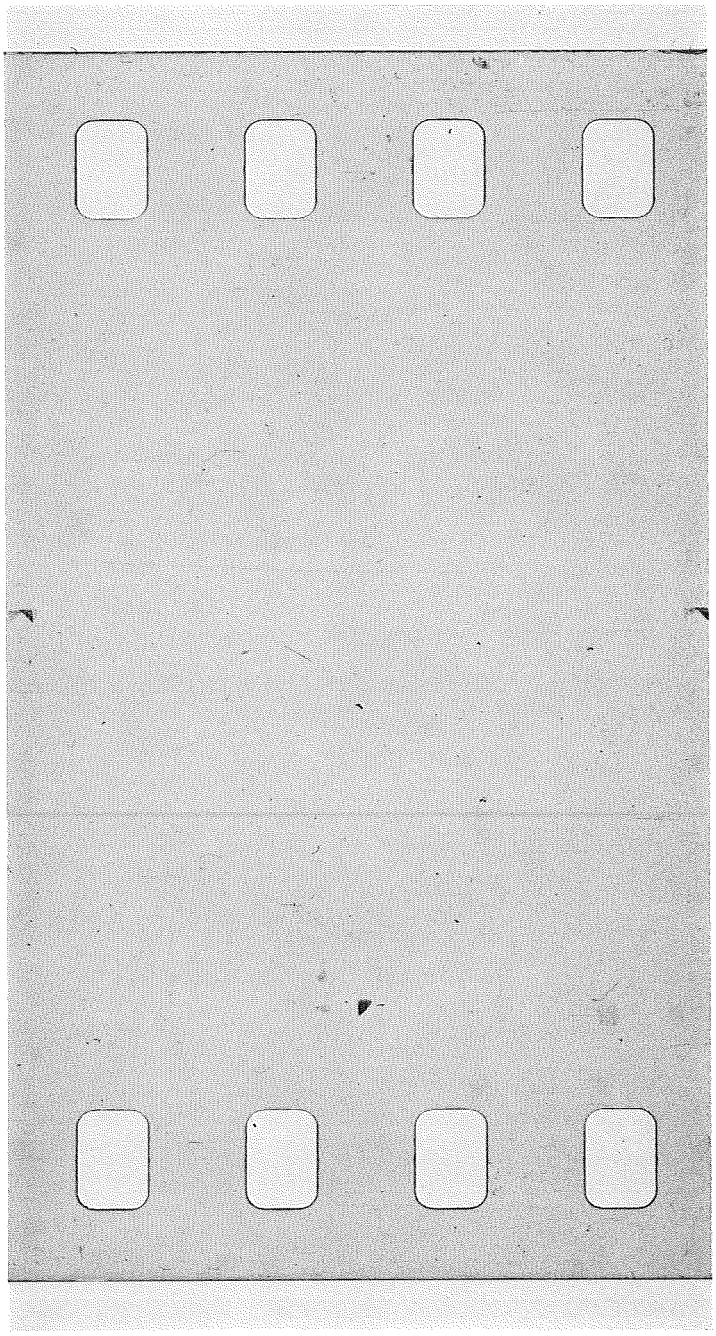

Figure 6-2 A frame from the flight x-ray image recording film showing the fiducial lights and the absence of scintillations from x rays.

7.0 SUPPLEMENTARY STUDIES

7.1 X-RAY REFLECTION STUDIES

7.1.1 Introduction

One of the major factors in determining the ultimate resolution of x-ray reflecting telescopes is the quality of the finish of the reflecting surfaces. The two major contributors to the surface finish are the large scale variations set by the tolerances imposed during the manufacturing process and the local irregularities or imperfections in the crystalline structure of the surface. An investigation of the latter is the scope of the present study.

The traditional Rayleigh criterion for a perfect reflecting surface is satisfied if surface irregularities introduce errors in the reflected wavefront of less than a quarter of a wavelength. For radiation incident at a grazing angle θ, the height h of a surface deviation corresponding to a $\lambda/4$ wavefront error is

$$h = \frac{\lambda}{8\theta}$$

For a wavelength of 8.3 Å and a grazing angle θ of 10, this gives a scale height of 60 Å. Irregularities of this scale and greater will modify the intensity distribution in the image plane on a scale of tens of arc seconds. Since the reflections occur at grazing incidence this redistribution occurs in an ordered way. Our studies have indicated that the rays scatter almost entirely in the plane of incidence of the incoming ray. This result is independent of whether the deviations are considered to arise from diffraction or specular reflection and depends only on the fact that the process takes place at grazing incidence. In either case analysis shows that the deviation of the incident rays perpendicular to the plane of incidence will be smaller than the deviation in the plane of incidence by the factor

$$\frac{\lambda\ \theta}{\Omega}$$

where Ω is a measure of the scale of the surface irregularities. This results from the foreshortening effect of grazing incidence.

The present study has been concerned with the irregularities which may be encountered on different surfaces and their effect on the scattered intensity distribution and reflection coefficient as a function of wavelength and angle of incidence.

7. 1. 2 Experimental Study of Scattered Intensity Distribution

The modification of the intensity distribution arising from the scattering process was studied by placing suitable flats in a beam of x-rays and measuring the spatial distribution of the scatterd photons. The x-rays are produced by electron bombardment of an aluminum target which generated a spectrum consisting of the characteristic aluminum Kα line at 8. 3 $\mathring{A}$ superimposed on a continuous bremmsstrahlung spectrum of reduced intensity with a low energy cut-off at approximately 4 $\mathring{A}$. These x-rays were collected and focused by a grazing incidence telescope having a focal length of 76 inches which was situated 720 inches from the source. A mask was placed over the telescope which allowed radiation to reach the focus only if it had been reflected from either one of two small regions on either side of the horizontal diameter of the telescope. A schematic diagram of the experimental set up is shown in Figure 7-1. The two reflections from the telescope will produce scattering in the plane of incidence which, in this case, is the horizontal direction. Consequently, the images at the focus will be fan shaped where the opening angle of the fan will be governed by the opening angle of the mask. These fans were further limited by placing defining slits, 30 mils wide, in front of the mask.

The optical flat to be tested was placed so as to intercept one of the converging beams and to deflect this beam vertically from its normal focus. In this way the scattering produced by the surface

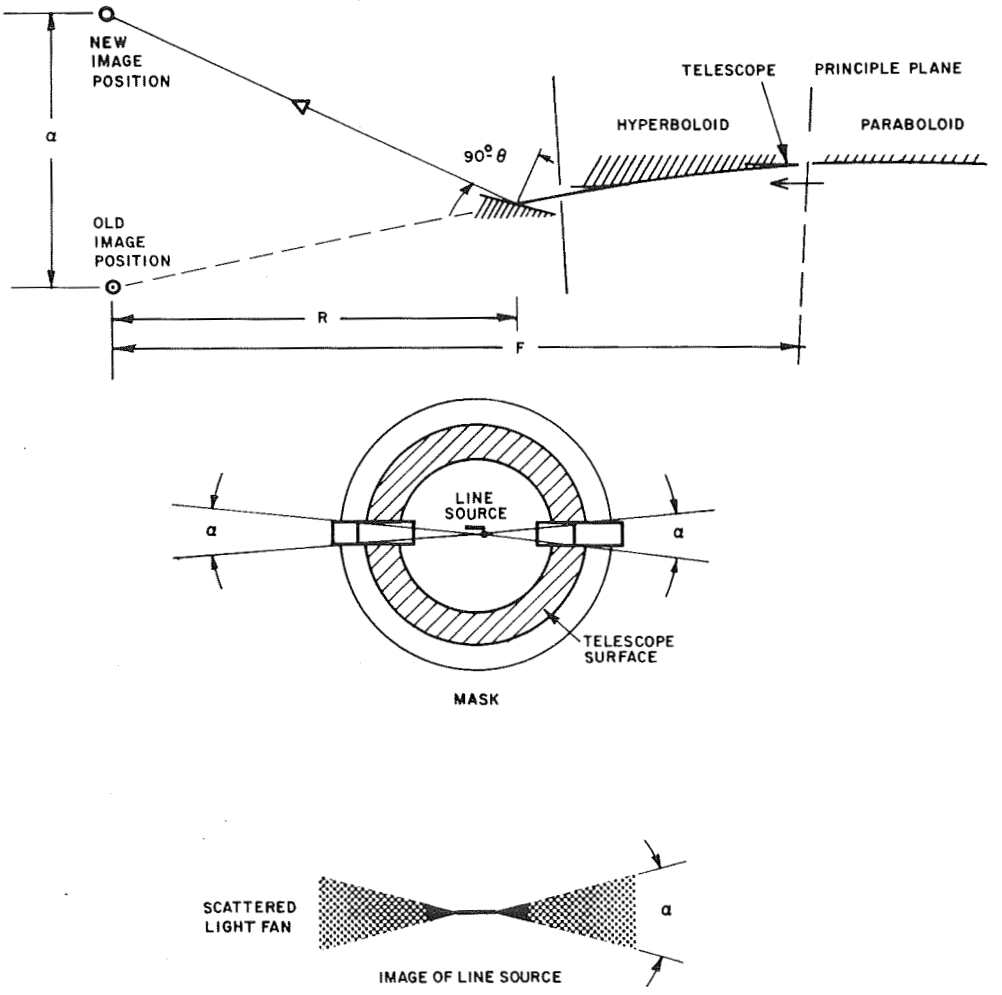

Figure 7-1 Schematic diagram of the experimental set up to measure the scattered intensity distribution.

irregularities of the flat will be perpendicular to the scattering produced by the telescope. If the grazing angle is θ, the vertical separation of the two images is given by

$$d = 2R\theta$$

for small θ and where d and R are defined in Figure 7-1.

In practice d and R are measured and the relation is used to calculate the grazing angle θ.

The initial measurements were made using a photographic technique. Both images were positioned using visible light on a single piece of 33 mm high speed film (Kodak #2485) before making an x-ray exposure. Although the qualitative features previously discussed were observed, the time required to make an exposure (~8 hours) was prohibitively long and the bulk of the measurements were made with proportional counters. These counters had 2 mil beryllium windows and were filled with P-10 (a mixture of 90% argon and 10% methane) at atmospheric pressure. One of the counters was fixed and was used to monitor the direct beam while the other was mounted on a movable table whose position was measured by a micrometer gauge. This counter was used to map out the intensity distribution of the reflected beam and to increase its spatial resolution it was provided with an adjustable slit which could be used to limit the field of view in the vertical direction. These measurements were performed in a vacuum chamber at a pressure not exceeding 1.0×10^{-5} mm Hg as the range of x-rays of these wavelengths in air is very small.

Two types of measurements were made. The first studied the variation of the intensity distribution from various surfaces at a constant angle of incidence, while in the second series of tests, the dependence of the scattering function upon the grazing angle was investigated for each type of material.

The results obtained for reflections at a grazing angle of 30 arc-minutes and using a slit size of 1 mil from glass (Cervit) and Kanigen (a nickel phosphorus alloy) are shown in Figures 7-2a and 7-2b, respectively. The ordinate in these figures is the ratio of the deflected beam to the undeflected beam, corrected for background and multiplied by 1000. This quantity is used to eliminate the effects of time variations in the source intensity. The full width at half maximum (FWHM) for the Kanigen flat is 27 arc-seconds and for the glass flat 14.5 arc-seconds. These values have to be corrected for the finite target and slit sizes. These corrections reduce the effective FWHM to 22.5 and 9.7 arc-seconds respectively. The difference cannot be accounted for by experimental uncertainties and must arise from physical differences in the two surfaces. On the other hand, a specially ion polished glass flat was indistinguishable from the Cervit flat.

Figure 7-3 shows the variation of the FWHM of the intensity distribution with grazing angle. The results show that the FWHM, $\Delta\phi$, of the distribution is directly proportional to the grazing angle, for the Cervit flat, namely,

$$\Delta\phi = k\theta$$

where the constant k is approximately equal to 1/2 if $\Delta\phi$ is measured in arc-seconds and θ in arc-minutes.

7.1.3 Electron Microscope Studies

Since the ion polished and the Cervit flats appeared to have the same scattering function and, by inference, similar scale surface irregularities, they were examined by electron microscope to determine whether differences could be detected. The electron micrographs were obtained by cleaning the flats and then forming a plastic (acetyl cellulose) replica. This replica was shadowed

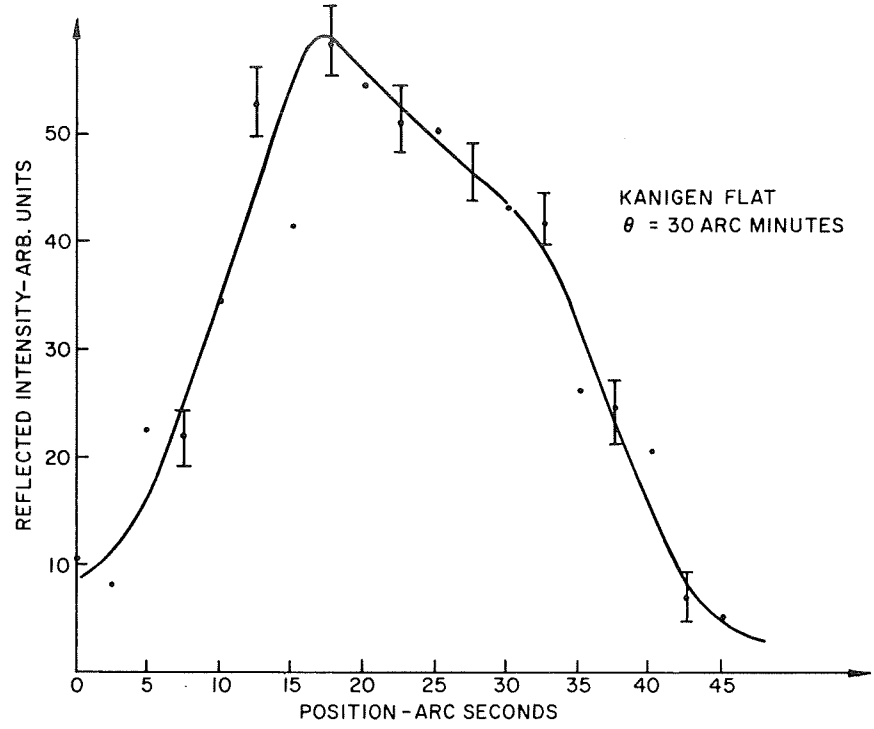

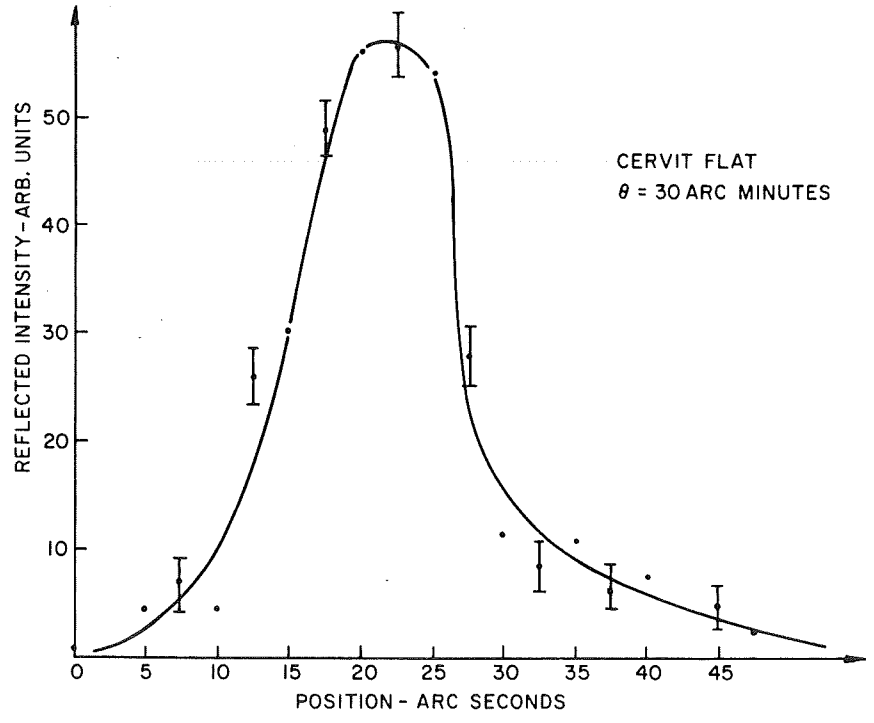

Figure 7-2 Scattered intensity distribution versus position for the Cervit and Kanigen flats.

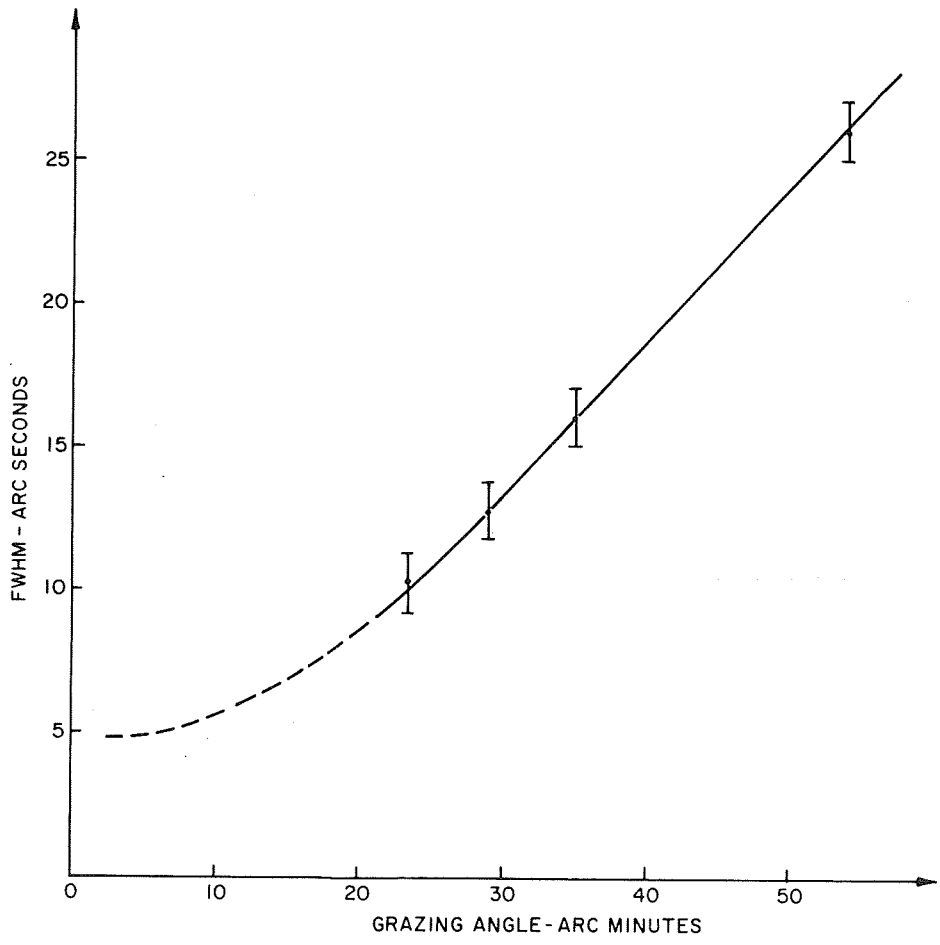

Figure 7-3 Variation of the FWHM of the scattered intensity distribution versus grazing angle for the Cervit flat.

at an angle of 5° with an evaporated platinum carbon mixture and then coated with a support film of carbon. The plastic was dissolved in acetone and the carbon film washed in acetone and then in water.

Although this procedure was chosen to produce the minimum grain size of the evaporated platinum, the size of the particles was too large to reveal any detail below 60 - 80 Å and at this resolution both flats appeared identical. The resulting photographs obtained at a magnification of 60,000 are shown in Figure 7-4.

7.1.4 Reflection Coefficients

Reflection coefficients of glass and acrylic plastic were made as a function of grazing angle and at two wavelengths. These measurements were made with the proportional counters and x-ray source previously described. The angle of incidence was varied by mechanically deflecting the flat and calculating the grazing angle from the measured deflection.

Figure 7-5 is a plot of the results of a study of uncoated glass using both 9.9 and 8.3 Å radiation. The material tested was microscope slide quality soda glass that is commercially available. No special handling or treatment procedures such as additional grinding or polishing of its surface were attempted prior to testing. As expected, the results show that the reflection efficiency is higher for the longer wavelength radiation and the qualitative behavior for both wavelengths are essentially the same. Acrylic plastic was also tested at 9.9 Å and the results are given in Figure 7-6. This sample was also a commercially available item that was not treated prior to testing. Its reflectivity at this wavelength is poorer than glass.

A further test was performed on a chromium coated sample of float glass and its efficiency appears to be much greater than that of

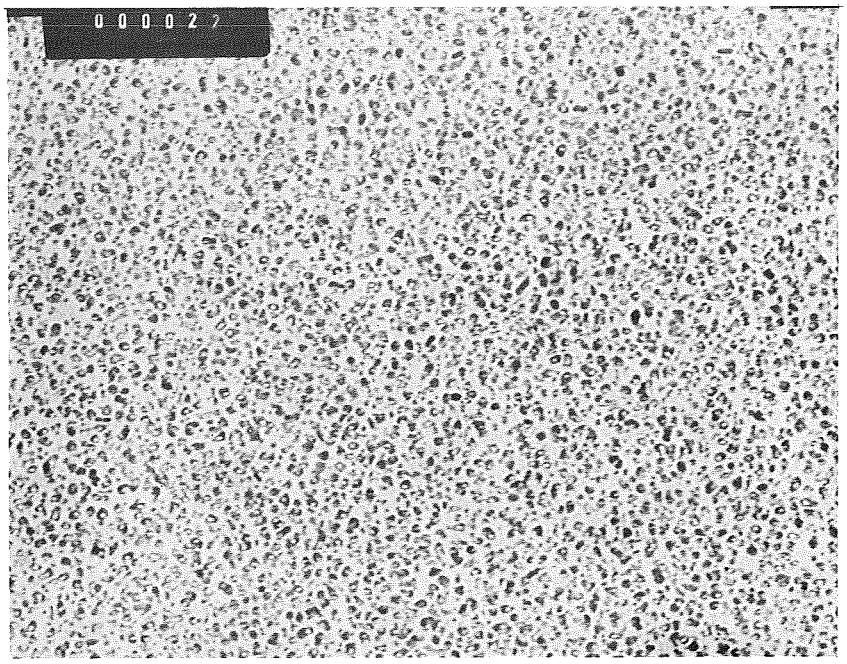

Ion-Polished Flat x 60,000

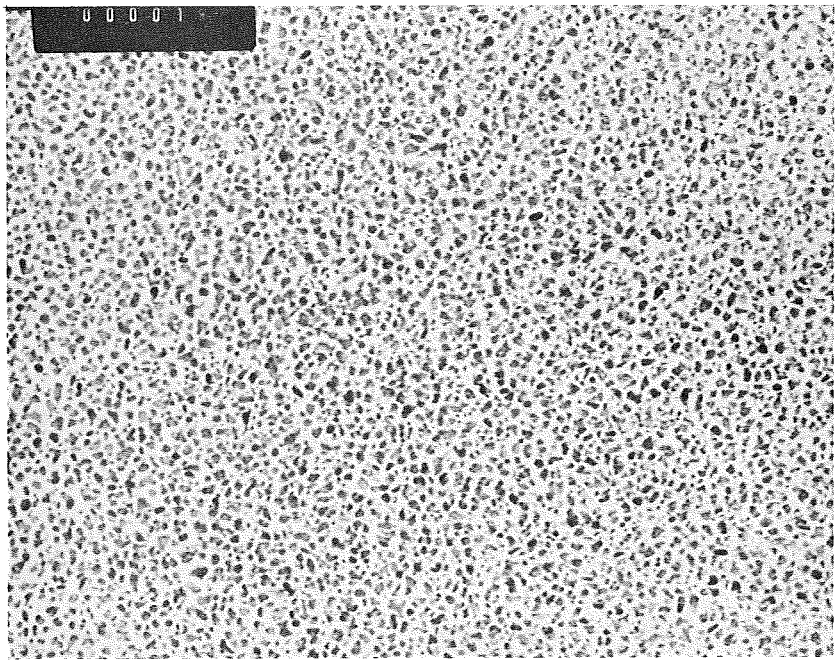

Cervit Flat x 60,000

Figure 7-4 Electron micrographs of the surface of the ion polished glass flat and the Cervit flat.

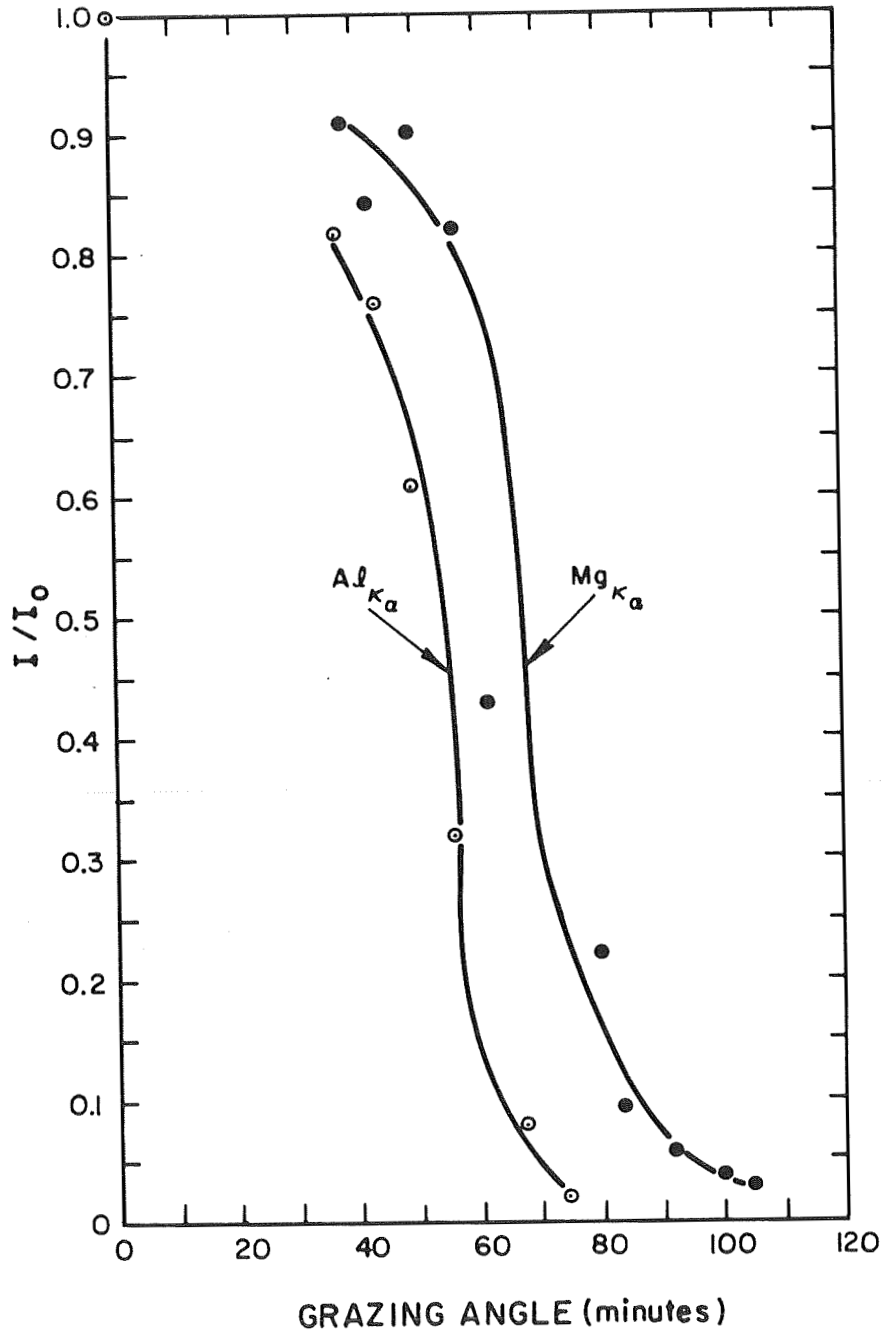

Figure 7-5 Grazing angle reflectivity of Glass for $Mg_{k\alpha}$ (9.88Å) and $Al_{k\alpha}$ (8.33Å).

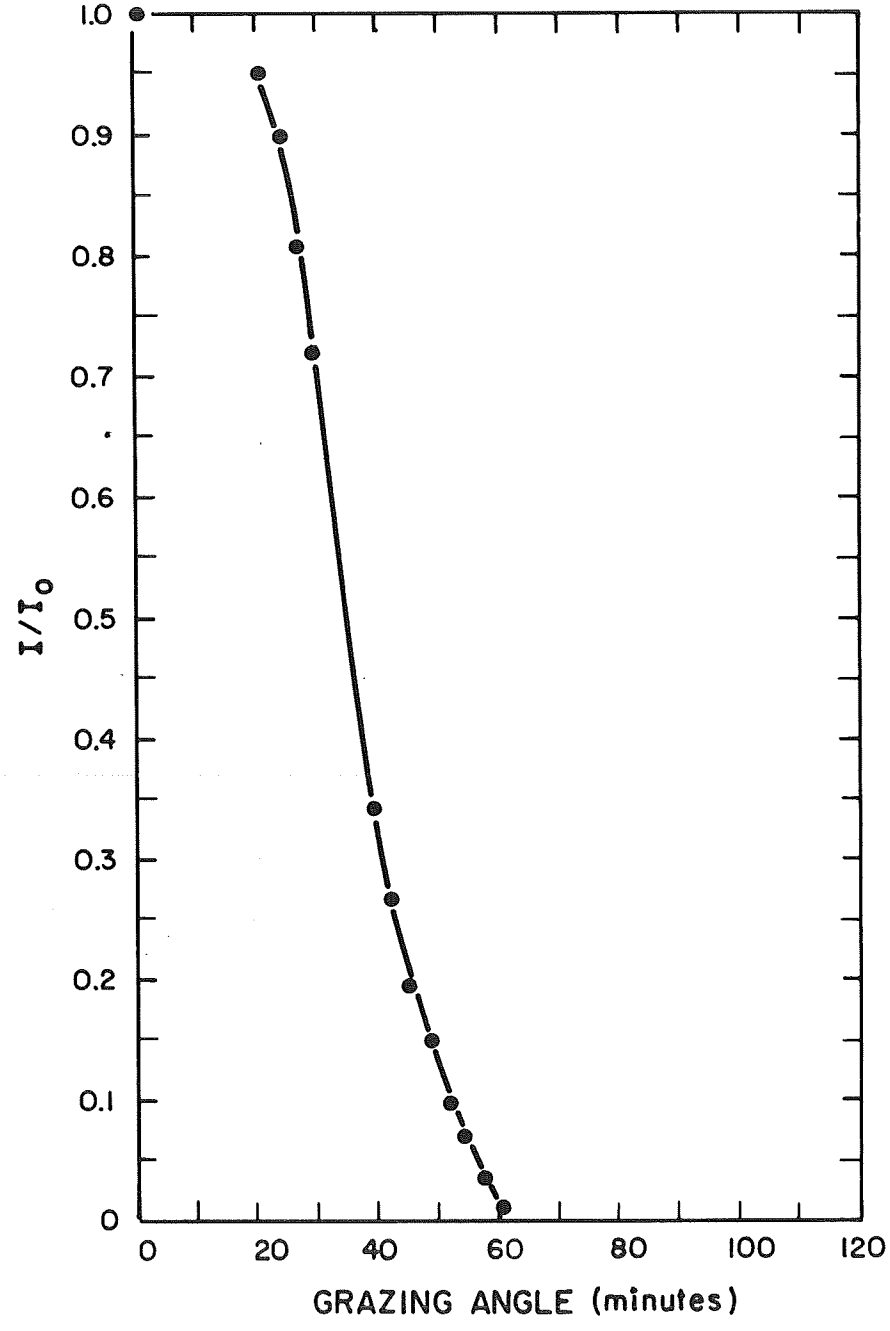

Figure 7-6 Grazing angle reflectivity of Acrylic plastic for $Mg_{k\alpha}$ (9.88 Å).

either the other samples (Figure 7-7). Superimposed on the curve are the results of measurements by Ershov et al. (Optics and Spectroscopy 22, 83, 1967) on the reflectivity of a polished chromium sample. The disagreement at the larger grazing angle could arise from a difference in the surface qualities of the two samples.

7.1.5 Conclusions

These tests have demonstrated that the Kanigen flats, as presently configured, produce considerably more scattering than optically polished glass. On the basis of the data obtained for the glass flats and with the assumption that the intensity distribution is of gaussian form then 80% of the radiation from a point source collected and focused by a grazing incidence telescope will fall within a circle of radius 17 arc-seconds.

The scale size of the irregularities which produce the scattering is less than 60 - 80 Å and it is possible that the improvements in the reflectivity of grazing incidence telescopes could result from coating optically polished glass with a high Z metal.

7.2 STELLAR AEROBEE 350 TELESCOPE PAYLOAD

A study was done in order to get a preliminary definition of an x-ray telescope payload for use with an Aerobee 350. In fact, we have considered two possible payloads. The A configuration has a high resolution Giacconi-Rossi mirror and an image intensifier detector. The B configuration has a high efficiency Baez mirror and an imaging proportional counter.

7.2.1 Typical Objectives

The A configuration can achieve:

a. Source locations to a few arc-sec of sources as weak as 10^{-4} Crab Nebula

b. High resolution picture of M87 containing 1500 counts

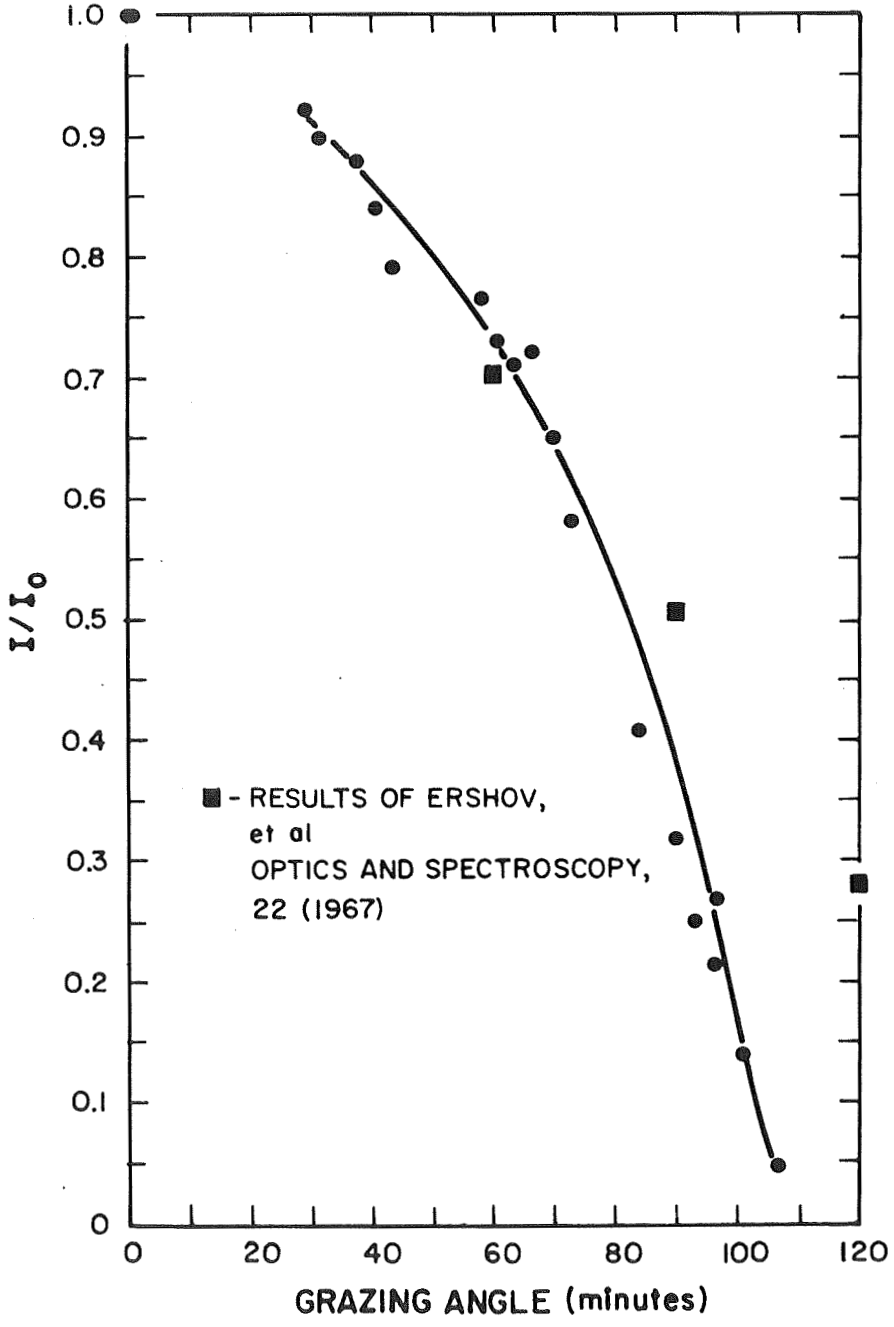

Figure 7-7 Grazing angle reflectivity of Chromium coated float Glass for $Mg_{k\alpha}$ (9.88 Å).

c. Observe lines in Sco X-1 spectrum to 0.05% of total flux, or in a 1/10 Sco X-1 source to 0.2% of total flux.

The B payload can survey at about 5 - 10 times the sensitivity of the A payload, with excellent long-wavelength sensitivity, but with only arc-minute resolution.

7.2.2 Program Requirements

The standard sounding rocket support provided by NASA will be required, including ACS using a STRAP system. The A payload will require a tracker which can be offset pointed, to about 10 arc-sec and a roll-axis stabilizer with a limit cycle of better than $\pm$ 1 arc min. Absolute pointing accuracy of 5 arc-min is required.

The B payload requires standard ACS support using STRAP III with presently achievable performance.

7.2.3 Payload Design

The basic payload configurations will be designed to accommodate the two different mirrors. Figure 7-8 shows the proposed design for the nested-pair paraboloid-hyperboloid mirrors. The design is similar to a payload system which is currently in process for the Aerobee 350 vehicle which is scheduled for flight in mid-1971. The current payload uses a single paraboloid-hyperboloid mirror system for solar x-ray imaging whereas the overall layout, mechanical structures, aspect system, star tracker, attitude control, and recovery systems will be applicable to the proposed sounding rocket payload.

The specifications of the two payloads are given in Table 7.2-1. Layout drawings of the payloads are shown in Figure 7-9 and 7-10.

A computer study of the performance of the high resolution and high efficiency mirror systems has been performed using a ray tracing program. The results are presented in Figures 7-11 through 7-14.

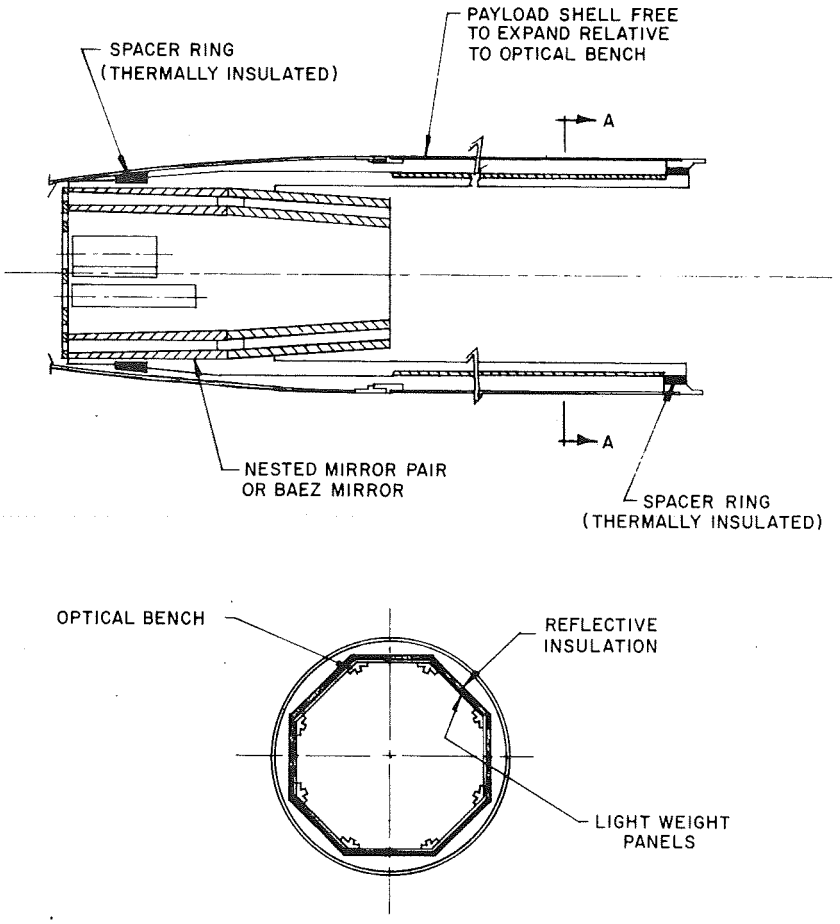

Figure 7-8 Payload A - optical bench and mirror mounts.

TABLE 7.2-1

Aerobee 350 Payload Specifications

A Payload

X-ray Optics Dimensions		
"	Focal Length	100 inches
"	Collecting Area	150 cm^2
"	λ cutoff	4 angstroms
"	Resolution	2 arc-seconds

Available Focal Plane

Volume	22 Diameter x 30 Long (6.5 cu. ft.) Module)
Power	As required
Weight	75 lbs. (approximate)
Overall Weight	450-500 lbs.
Telemetry Requirements	S-Band; ~ 16 channels
Timed Functions	~ 10
Pointing Capability	$\pm$ 2 min.
Peak Altitude	335Km
Time-to-Peak Altitude	308 sec.
Time above 100 Km	425 sec.

TABLE 7.2-1 (Continued)

B Payload

X-ray Optics Dimensions	
" Focal Length	108 inches
" Collecting Area	300 cm^2
" λ cutoff	5 angstroms
" Resolution	20 arc-seconds
Available Focal Plane	
Volume	22 Diameter x 20; (4.3 cu. ft.)
Power	As required
Weight	75 lbs. (approximate)
Overall Weight	450-500 lbs.
Telemetry Requirements	S-Band; 16 channels
Timed Functions	~10
Pointing Capability	$\pm$ 2 min.
Peak Altitude	335 Km
Time-to-Peak Altitude	308 sec.
Time above 100Km	425 sec.

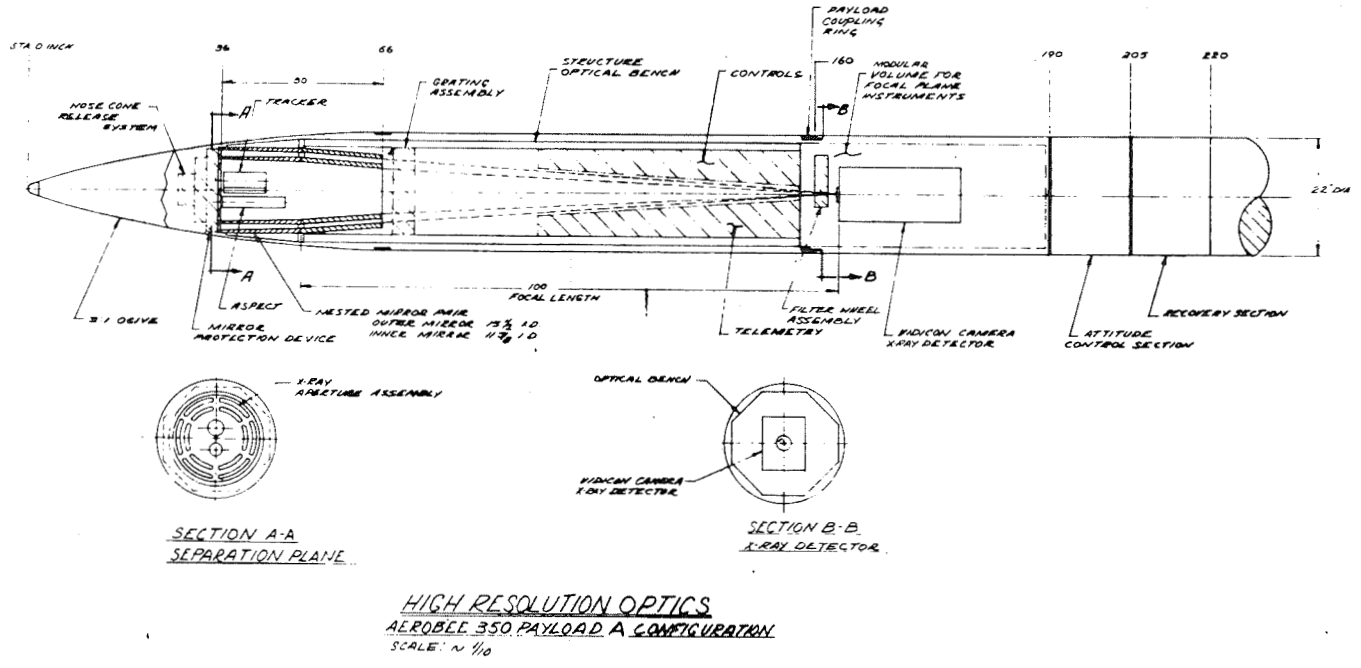

Figure 7-9 Layout drawing of the high resolution payload.

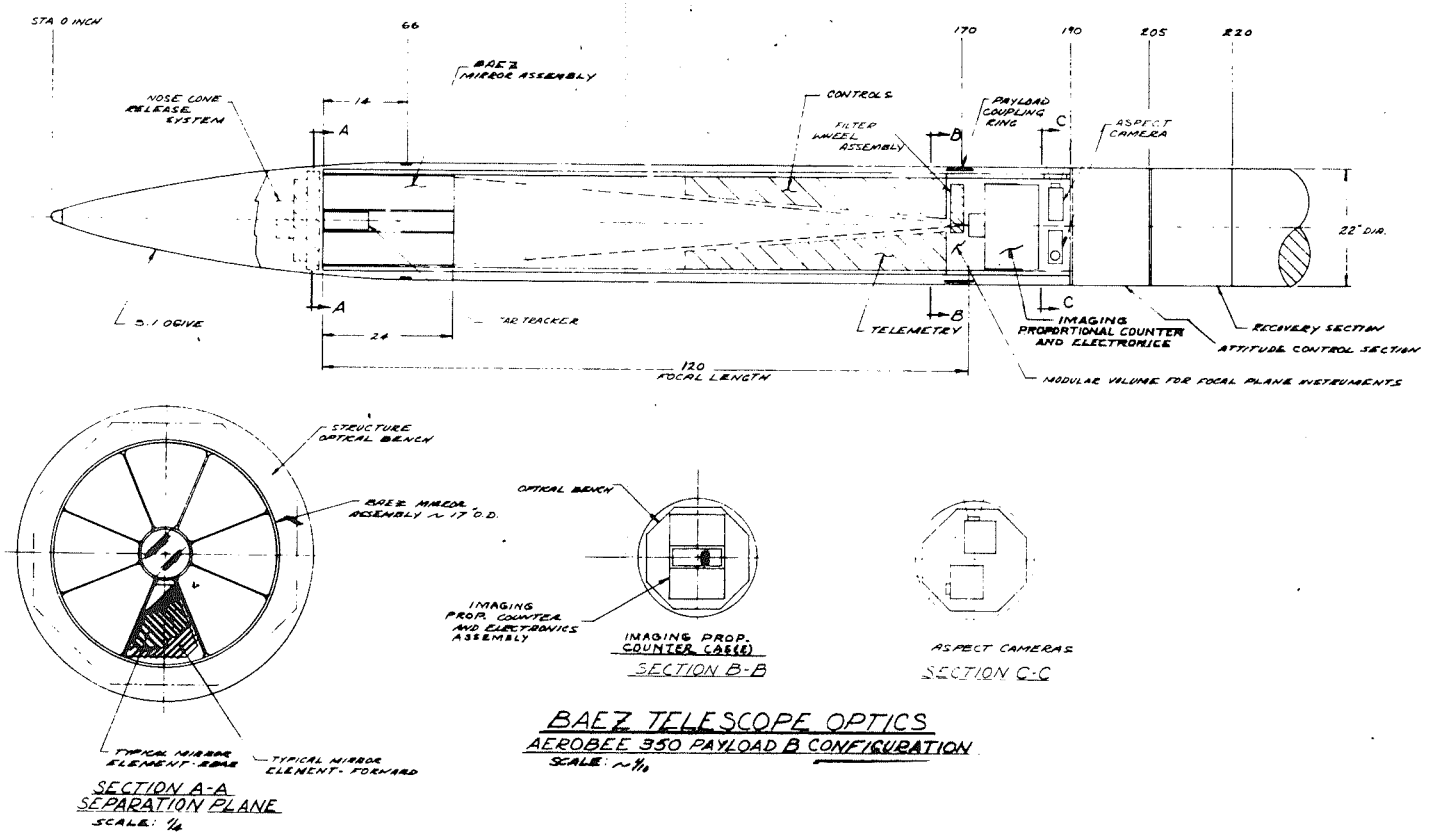

Figure 7-10 Layout drawing of the high efficiency payload.

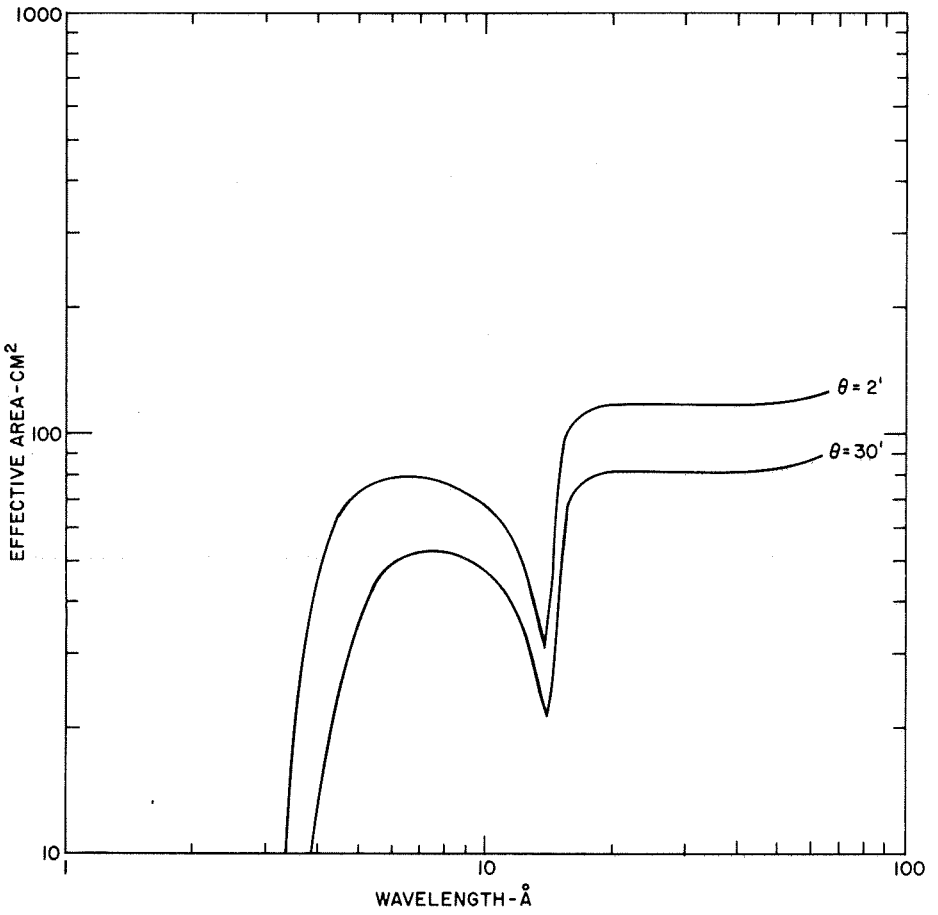

Figure 7-11 Effective area versus wavelength at two angles of incidence for the high resolution mirror.

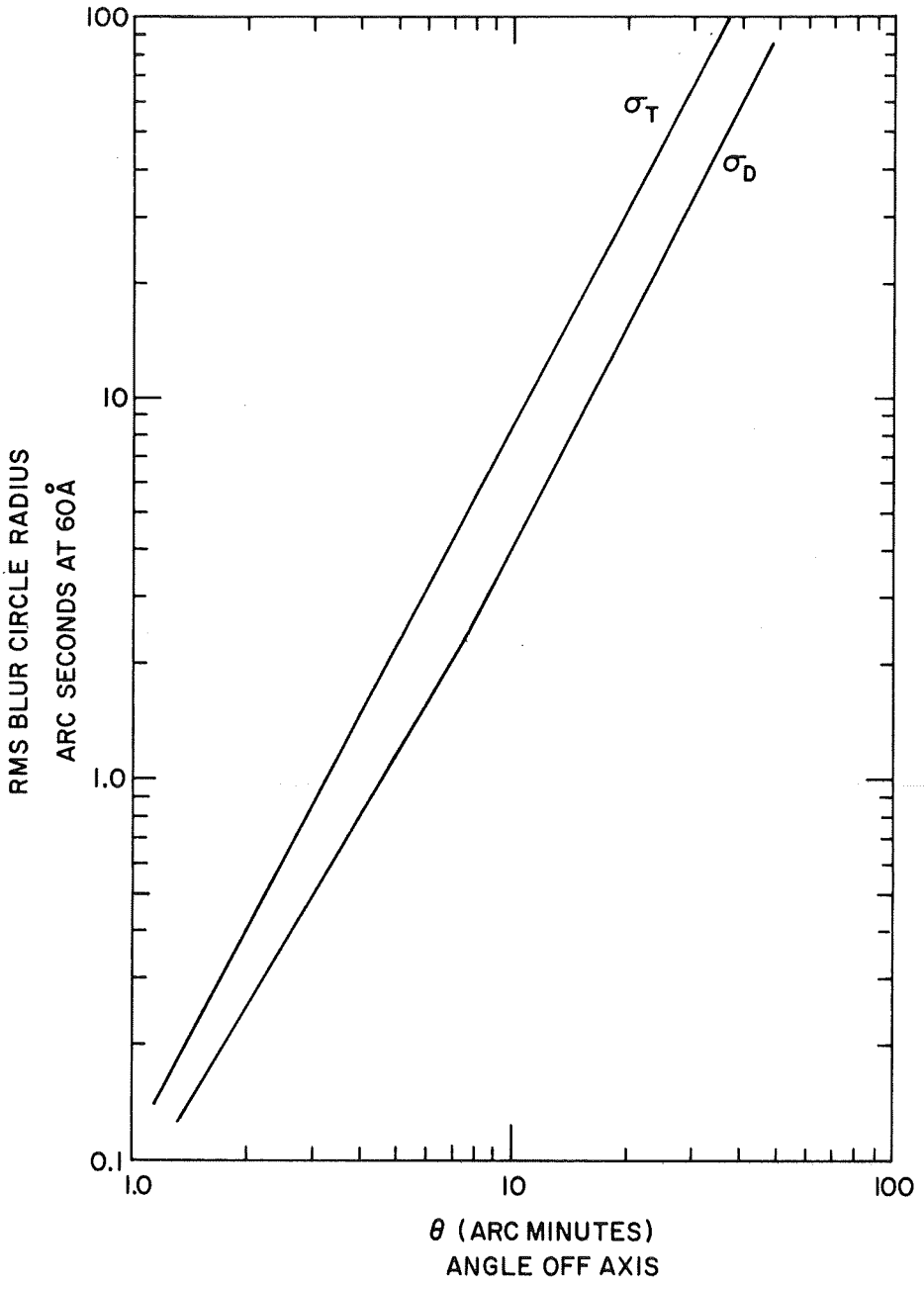

Figure 7-12 RMS radius of the blur circle at 60 Å versus the angle of incidence for the high resolution mirror. The curve labeled σ_T is for a flat focal plane while the curve σ_D is for an optimally curved focal plane.

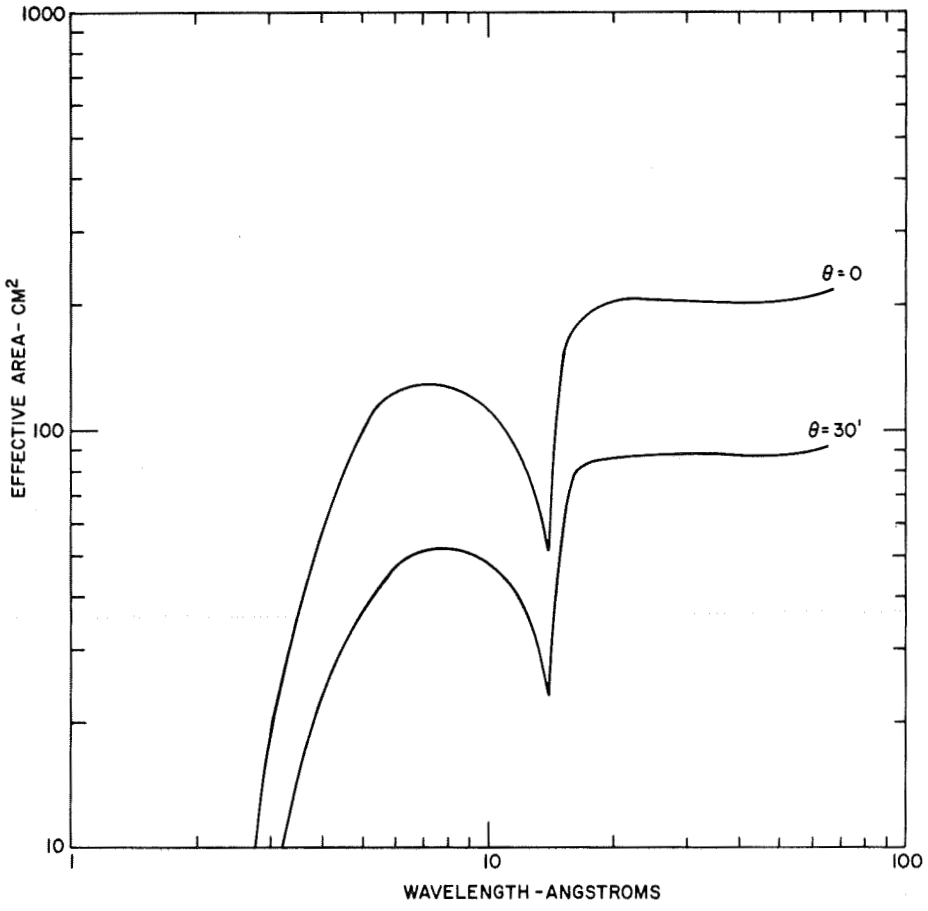

Figure 7-13 Effective area versus wavelength at two angles of incidence for the high efficiency mirror.

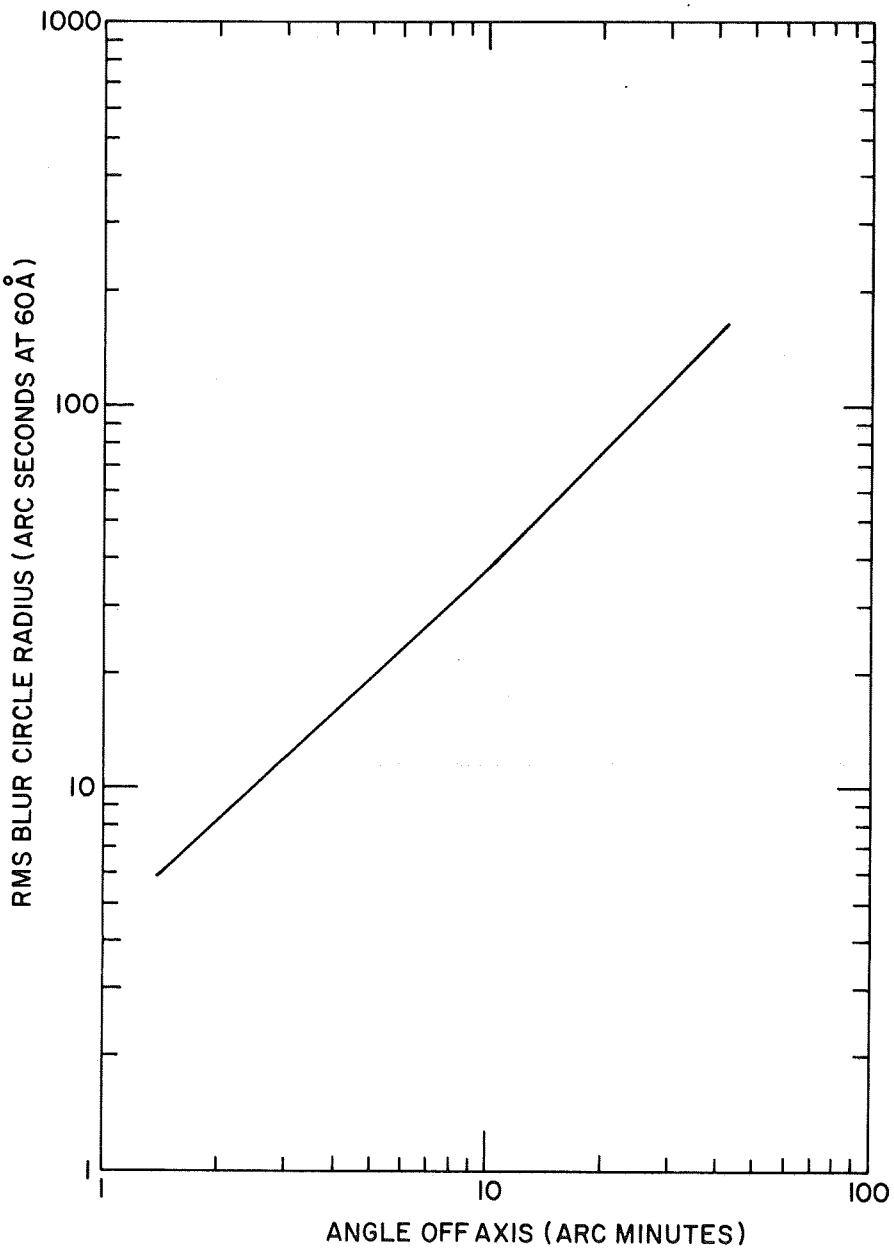

Figure 7-14 RMS radius of the blur circle at 60 Å versus the angle of incidence for the high efficiency mirror.

The sample of rays traced through the two systems was large enough to insure that the RMS error in the effective area was less than 5% in each case. Figure 7-11 shows the results of the calculation of the effective area of the high resolution mirror payload A, as a function of wavelength for different angles of incidence. Figure 7-12 shows the RMS radius of the blur circle as a function of angle of incidence for this same mirror. The two curves in Figure 7-12 represent the blur circle for a flat and an optimally curved focal plane, labeled σ_T and σ_D respectively. Figures 7-13 and 7-14 present the same data for the high efficiency telescope, payload B. Note, in reference to Figure 7-14, that for the Baez geometry a flat focal plane is essentially an optimal focal plane.

7.3 VEHICLE PERFORMANCE

Estimated payload weight is 475 lbs. and apogee is estimated to be about 335Km for 87° elevat on sea level launch. For WSMR launch (4000 feet elevation), we obtain approximately 3 to 5 per cent higher apogee. Figure 7-15 shows trajectory performance data for the Aerobee 350 vehicle. Total flight time will be approximately 10.25 minutes and flight time above 100 Km will be about 7.25 minutes.

It is interesting to compare the effective exposure time of the A payload with that of the Aerobee 150 payload described earlier in this report.

	Aerobee 150	Aerobee 350 A Payload
Projected Area	35 cm^2	150 cm^2
Reflection Efficiency	0.03	0.06
Time	200 sec	435 sec
AT	210 cm^2-sec	3915 cm^2-sec

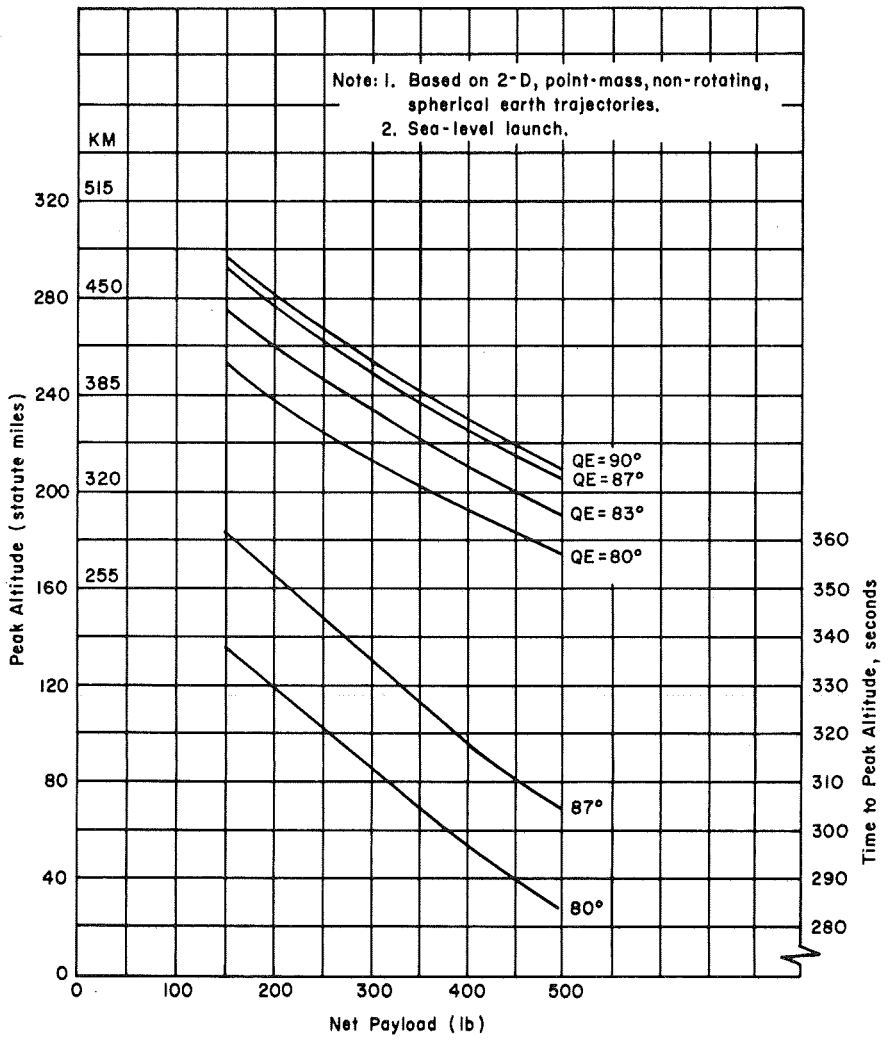

Figure 7-15 Expected performance of the Aerobee 350 rocket.

This estimate assumes only a factor of two improvement in reflection efficiency for the 350 A Payload mirror. The reflection efficiency is defined operationally as the fraction of energy from a point source at infinity reflected into one resolution element. Thus, the choice of Cervit for the 350 A mirror will probably give us better than a factor of two improvement over the Kanigen mirror used in the Aerobee 150 payload, due to its better scattering properties, as well as its greater bulk coefficient of reflection. We can expect that the 350 A telescope will give more than the factor of 18.6 increased performance calculated on page 7-24.